August 2023

Exploring New Physics Through Collider and Gravitational Wave Measurements with Artificial Neural Networks: the Case Study of QCD-like Technicolor

Ashar Kamal

Department of Astronomy and Theoretical Physics, Lund University

Master thesis supervised by Roman Pasechnik
and co-supervised by António Morais

LUND
UNIVERSITY

Abstract

With physicists actively exploring Beyond the Standard Model (BSM) theories that may fill in the gaps of the Standard Model (SM), a fundamental question arises: which parameters hold physical significance? In this thesis, we present our initial progress towards the development of a model-independent artificial intelligence framework designed for conducting parameter space scans in BSM scenarios. Our framework incorporates several publicly available high-energy physics packages, namely `SPheno`, `HiggsBounds`, `HiggsSignals`, and `CosmoTransitions`. These packages enable us to impose various constraints including unitarity, electroweak precision, Higgs exclusion limits, and strong detectable first-order cosmic phase transitions. To demonstrate the effectiveness of our framework, we apply it to a singlet-triplet extended SM, serving as a minimal low-scale effective field theory for a quantum chromodynamic-like Technicolor (TC) theory. A proper phenomenological investigation and parameter space analysis of the TC theory in the UV-limit are planned for future work. The findings from our preliminary investigation exhibit promising results, demonstrating a substantial efficiency enhancement when compared to conventional random search approaches for identifying physically relevant parameter points. These outcomes pave the way for future BSM studies utilizing our developed framework.

Populärvetenskaplig beskrivning

Standardmodellen är idag fysikens mest konkreta beskrivning av universums minsta beståndsdelar. Den tillåter oss att kategorisera den synliga materian i sina grundläggande partiklar och beskriva deras växelverkan genom tre av de fyra fundamentala naturkrafterna; elektromagnetism, den starka kraften och den svaga kraften. Modellen har även lyckats förena beskrivningen av elektromagnetism och den svaga kraften till en och samma teori, som kallas den elektrosvaga teorin. Den elektrosvaga teorin spelar en väsentlig roll i Higgsmekanismen, vilket är den mekanism som genererar massa åt många av de fundamentala partiklarna i Standardmodellen.

Trots stora framgångar med Standardmodellen finns det fortfarande fenomen som den inte kan förklara. Ett exempel är de kosmologiska observationerna som visar att det finns en betydligt större andel materia än antimateria i universum. Ett annat exempel är vad som i grunden driver Higgsmekanismen från första början. Eftersom modellen inte kan besvara dessa frågor, tyder det på att det finns ny fysik bortom Standardmodellen.

Därför föreslås det regelbundet utökade modeller med fler partiklar och interaktioner, vilket också bidrar till flera nya parametrar. En naturlig fråga blir då: vilka värden ska de nya parametrarna ha för att ge en giltig fysikalisk teori? Eftersom många parametervärden förutspår fysik som inte kommer överens med observationer från partikelacceleratorer och kosmologi blir många värden för parametrarna uteslutna, och en slumpmässig sökning blir mycket tidskrävande. För att underlätta sökningen har vi utvecklat ett program som använder sig av artificiell intelligens i form av ett neuralt nätverk. Målet är att låta nätverket rekommendera parametervärden som den anser är bra, i hopp om att sannolikheten för att hitta bra parametervärden går upp. Effektiviteten av nätverket testas genom att tillämpa den på en förenklad modell, baserad på den mer komplicerade ”Technicolor” modellen. När nätverket anses vara tillräckligt effektivt, planeras den att tillämpas på Technicolor modellen och andra fysikaliskt relevanta modeller. gma

Contents

List of acronyms

AI	Artificial Intelligence
ANN	Artificial Neural Network
BAU	Baryon Asymmetry of the Universe
B(SM)	Beyond the (Standard Model)
CHM	Composite Higgs Model
(C)P	(Charge-)Parity
EFT	Effective Field Theory
(EW)SB	(Electroweak) Symmetry Breaking
EWB	Electroweak Baryogenesis
FO(PT)	First-order (Phase Transition)
GW	Gravitational Wave
HEP	High-energy Physics
KDE	Kernel Density Estimation
LσM	Linear Sigma Model
PDF	Probability Density Function
QCD	Quantum Chromodynamics
STESM	Singlet-Triplet Extended Standard Model
SNR	Signal-to-noise-ratio
TC	Technicolor
VEV	Vacuum Expectation Value

1 Introduction

The Standard Model (SM) is the most accurate description of our present knowledge of the universe at microscopic distances. It lets us organize visible matter into its most fundamental structures and describe their interactions via the electromagnetic, weak and strong forces. One of its most impressive feature is its joint description of the electromagnetic and weak theories into one single theory, the electroweak (EW) theory. The subsequent breaking of the EW symmetry is then used to describe how the SM quarks, charged leptons and vector bosons acquire their mass, known as the Higgs mechanism [1, 2]. Nevertheless, despite its remarkable achievements, the SM is still an incomplete theory, some of its most imminent shortcomings include a missing description of gravity, predicting zero neutrino masses at a renormalizable level and failing to predict the observed Baryon Asymmetry of the Universe (BAU) [3]. This has lead to various proposed extensions of the SM.

The matter-antimatter dilemma has long been a mystery of Particle Physics. Assuming an initially symmetric universe (baryon number $B = 0$), the observed imbalance must be attributed to some baryon-generating process. This phenomenon is referred to as baryogenesis, and the necessary conditions for it to occur were first formulated by Andrei Sakharov in 1967 [4]. One way to realize Sakharov's conditions and enable baryon-generating processes is through a cosmic phase transition characterized by bubble nucleation, referred to as a First-order Phase Transition (FOPT). Additionally, the FOPT must be of sufficient strength to avoid the asymmetry being washed out through reverse processes [5]. The EW phase transition, which describes the transition of the universe from a state that respects $\mathrm{SU(2)_W} \times \mathrm{U(1)_Y}$ symmetry to a broken state, is commonly used to explain the BAU. However, the measurement of the Higgs mass at $m_\mathrm{h} = 125.25$ GeV [6] has ruled out a first-order EW phase transition within the SM alone [7].

Another concern regarding the SM is the origin of its Electroweak Symmetry Breaking (EWSB). Currently, it is postulated that the Higgs field's mass parameter μ_H^2 is negative at the EW-scale, leading to the EW symmetry spontaneously breaking. However, no underlying reason is given to what drives μ_H^2 to negative values in the first place. Furthermore, during this process, the Higgs acquires a VEV $v = 246$ GeV, but the fundamental reasons for this particular VEV also remain unknown [8].

One possible way of addressing the latter concern is by incorporating the Quantum Chromodynamic (QCD)-like extension of the SM, known as Technicolor (TC). TC is a strongly coupled $\mathrm{SU(N_{TC})}$-based gauge theory, where $\mathrm{N_{TC}}$ is the number of technicolor charges. The theory contains $\mathrm{N_{TC}^2} - 1$ 'techni-gluon' gauge bosons (T-gluons) and $\mathrm{N_f}$ non-chiral, or vector-like, 'techni-quarks' (T-quarks). One advantage of the vector-like nature of the T-quarks is that it provides a "natural" way for them to attain mass without relying on the Higgs mechanism, giving the theory a certain elegance. At energy scales around $\Lambda_\mathrm{TC} \sim \mathcal{O}(1 - 100\ \mathrm{TeV})$, TC exhibits a phenomenon called technicolor confinement. In

complete analogy to QCD, below its confinement scale, the theory predicts bound states, including T-baryons (combination of T-quarks) and T-mesons (pairs of T-quarks and T-antiquarks).

The main feature of the theory is its composite Higgs sector, consisting of the $\mathcal{H}$ and $\mathcal{K}$ iso-doublets, with the components being T-mesons. Chiral symmetry $\mathrm{SU(N_f)_L \times SU(N_f)_R}$ (R for right and L for left) is broken explicitly at $\mathcal{O}(1 - 100$ TeV) by supplying the techni bound state σ with a non-zero vacuum expectation value (VEV). Since TC phenomenology is not the primary focus of this thesis, a minimal EW-scale Effective Field Theory (EFT) inspired by TC will be adapted. In this simplified EFT, we make the assumption that the Higgs mass term flows towards negative values due to radiative corrections, triggering the EWSB spontaneously. In a SM-like way, the breaking is characterized by the Higgs field $\mathcal{H}$ acquiring a VEV at $\langle \mathcal{H} \rangle = \frac{1}{\sqrt{2}} \begin{pmatrix} 0 \\ v \end{pmatrix}$ with $v = 246$ GeV.

With the emergence of new BSM theories, a natural question arises concerning the required values of the Lagrangian parameters for achieving a physically viable theory. Addressing the BAU requires the presence of strong FOPTs, preferably accompanied by detectable Gravitational Waves (GWs). These constraints can be characterized by the amount of energy released by the phase transition and the amplitudes of the resulting GWs, respectively. Naturally, the theory must also satisfy constraints imposed so far by high-energy colliders such as the LHC and other experimental facilities. The parameter space is therefore further constrained when taking into account the impact of collider observables. In this respect, for the purposes of this thesis, we consider the EW precision observables introduced by Peskin and Takeuchi [9, 10], commonly referred to in literature as the oblique parameters. These parameters characterize the impact of the new physics in the radiative corrections of the SM gauge bosons. Additionally, we also take into account the most up-to date constraints set by direct Higgs searches, including exclusion limits on production and decay channels [11, 12]. On the theoretical side, tree-level unitarity is incorporated to the network, which is related to the conservation of probabilities in scattering processes [13].

To the best of our knowledge, there is currently no publicly available framework that efficiently performs large-scale parameter scans for collider and cosmic constraints. This is the motivation behind our proposition of constructing a framework that utilizes Artificial Neural Networks (ANNs) for faster probing of BSM parameter spaces for such constraints. The objective of the ANN is to suggest which regions of parameter space to scan, in an attempt to increase the low accuracy associated with random search. Once the framework is built, it will be applied to the EW-scale EFT, serving as our toy model. The primary focus of this thesis lies on creating and improving the parameter space scanner, while giving less attention to phenomenology that is unrelated to the framework's development.

The structure of this thesis is as follows. In Sec. 2, the UV-complete TC theory and the Compose Higgs Model (CHM) within it are formulated, from which we take inspiration to construct the EW-scale EFT toy model. The theoretical constraints are laid out and the low-scale theory is implemented using the `SARAH Mathematica` package [14, 15, 16]. In Sec. 3, the collider constraints and the theory behind them will be covered. This includes Higgs search exclusion limits from the LHC, LEP and Tevatron experiments, using `HiggsBounds` [17, 18, 11] and `HiggsSignals` [19, 12], as well as constraints imposed by the Peskin-Takeuchi parameters. Properties such as STU parameters and particle masses, will be calculated through the use of `SPheno` [20, 21]. Following, in Sec. 4, the cosmic constraints are looked into. FOPTs are identified by numerically evaluating the bounce action, which is done by the `CosmoTransitions` package [22]. On the other hand, the thermal effective potential of the theory is constructed via dimensional reduction using `DRalgo` [23]. In Sec. 5 the structure of the developed framework is specified. The High-energy Physics (HEP) packages are tied together into a `Python` script, and a machine learning algorithm is defined to scan through the model input parameter space against the constraints defined above. In Sec. 6, the framework is applied to the toy model and results are presented. Finally, concluding remarks are made in Sec. 7.

2 Constructing the Technicolor Model

2.1 Composite Higgs models

A popular method of retaining EWSB while avoiding the introduction of a scalar Higgs particle into the theory is by extending the SM by a new strongly coupled gauge theory. This new sector will include a set of new fundamental particles, from which a Higgs bound state can be constructed with the constraint that its mass and quantum numbers match the experimentally observed Higgs boson. In addition, the mass-generating description for SM fermions and bosons must be updated to account for the compositness of the new model. Such CHMs are introduced as following: The strongly coupled gauge sector and associated interactions within the new theory are added to the SM Lagrangian (excluding the SM Higgs boson). The two sectors may then be connected by introducing interaction terms between them. Schematically, we arrive at [24]

$$\mathcal{L}_{\mathrm{SM}} \to \mathcal{L}_{\mathrm{SM}_0} + \mathcal{L}_{\mathrm{s}} + \mathcal{L}_{\mathrm{port}},$$

where $\mathcal{L}_{\mathrm{SM}}$ is the SM Lagrangian, $\mathcal{L}_{\mathrm{SM}_0}$ the SM Lagrangian excluding the SM Higgs boson, $\mathcal{L}_{\mathrm{s}}$ belongs to the strongly coupled gauge theory and $\mathcal{L}_{\mathrm{port}}$ is the portal between the SM and the new gauge theory, describing interactions between the two sectors.

For the portal between TC and the SM, a minimalistic approach is taken here, where the unknown $\mathcal{L}_{\mathrm{port}}$ in the UV-limit triggers the SM-like Yukawa interactions of the composite Higgs sector and elementary SM fermions. Due to the compositeness of the exotic Higgs boson, at the fundamental level this would require interaction terms between the T-quarks and the SM quarks, charged leptons and vector bosons. In our simplified description, we assume that the exotic Higgs sector interacts with the SM in the ordinary SM-like way, without delving into the associated UV-complete theory phenomenology. The gauge group of the full model is $\mathrm{SU(N_{TC})_{TC}} \times \mathrm{SU(3)_C} \times \mathrm{SU(2)_W} \times \mathrm{U(1)_Y}$, where, C is color, W is weak and Y indicates hypercharge.

Before constructing the chirally symmetric Lagrangian, which is done using a method called the Linear Sigma Model (LσM), a slight detour is taken into chiral symmetry breaking in QCD. Although the source of the (explicit) symmetry breaking in QCD is different from ours, the dynamics are very similar and valuable insight can be gained by looking at the SM case first.

2.2 Chiral symmetry breaking in QCD

Typically, the flavours are divided into light quarks (u, d and s) and heavy quarks (c, b and t). In the low-energy QCD limit ($\ll m_c$, where m_c is the charm quark mass), the QCD

Lagrangian may be approximated by its light quark flavours

$$\mathcal{L}_{\mathrm{QCD}} = \sum_{f=u,d,s} \bar{q}_f (i\not{D} - m_f) q_f - \frac{1}{4}\mathcal{G}^a_{\mu\nu}\mathcal{G}^{\mu\nu}_a = \\ = \sum_{f=u,d,s} \bar{q}_{f,\mathrm{L}} i\not{D} q_{f,\mathrm{L}} + \bar{q}_{f,\mathrm{R}} i\not{D} q_{f,\mathrm{R}} - m_f(\bar{q}_{f,\mathrm{L}} q_{f,\mathrm{R}} + \bar{q}_{f,\mathrm{R}} q_{f,\mathrm{L}}) - \frac{1}{4}\mathcal{G}^a_{\mu\nu}\mathcal{G}^{\mu\nu}_a \tag{2.1}$$

In the last step the fermionic fields have been split up into their chiral components. Here, f runs over the light quark flavours, q_f is a color triplet and a is an index that runs over the adjoint representation of SU(3). For simplicity of the presentation we have omitted the colour indices for the quark fields. The covariant derivative is defined in the usual way $D_\mu = \partial_\mu - ig_s(\lambda_a A^a_\mu)$ where g_s is the strong coupling constant, λ_a are the Gell-Mann matrices and A^a_μ is the gluon field. The field stress tensor is defined as $\mathcal{G}^a_{\mu\nu} = \partial_\mu A^a_\nu - \partial_\nu A^a_\mu - g_s f^a{}_{bc} A^b_\mu A^c_\nu$ where f is the SU(3) structure constant. We have also introduced the Feynman slash as $\not{A} \equiv A^\mu \gamma_\mu$.

It is straightforward to prove that the above Lagrangian is invariant under the chiral $\mathrm{SU(3)_L} \times \mathrm{SU(3)_R}$ transformation

$$q_L \to U_L q_L \,, \\ q_R \to U_R q_R \,,$$

in the chiral limit $m_u = m_d = m_s = 0$. U_L and U_R are special unitary 3×3 matrices independent from each other. Although the up, down and strange quarks are not massless, their relatively small masses still leave the chiral symmetry an approximate symmetry [25].

During spontaneous chiral symmetry breaking, $\mathrm{SU(3)_L} \times \mathrm{SU(3)_R}$ is broken down to the flavour $\mathrm{SU(3)_V}$ group and manifests itself by producing eight Nambu-Goldstone bosons. One way of breaking the symmetry spontaneously in the QCD chiral limit is via the formation of a non-vanishing flavour-diagonal quark condensate $\langle \bar{q}q \rangle$. Since chiral symmetry is not an exact symmetry of the low-scale QCD Lagrangian, the non-invariant mass terms induce an explicit symmetry breaking on top of the spontaneous one, effectively turning the massless Goldstone bosons into massive pseudo-Goldstone bosons [26].

2.3 Linear sigma model

The TC theory considered in this thesis relies on the Linear Sigma Model description to break chiral symmetry explicitly, similarly to QCD producing massive T-mesonic pseudo-Goldstone bosons. For now, these bosons may be thought of as regular QCD mesons. In this approach, the source of the explicit symmetry breaking comes from Yukawa T-quark-meson interactions. Below, we summarize the treatment given in [27] on how to construct

a chirally symmetric Lagrangian in the two-flavour case using the LσM.

We extend the original massless Lagrangian by adding the fermion-meson interaction terms via

$$\mathcal{L}_{\text{int}} = -\bar{\psi}_{\text{L}} M \psi_{\text{R}} - \bar{\psi}_{\text{R}} M^{\dagger} \psi_{\text{L}} \,, \tag{2.2}$$

where $\psi = \begin{pmatrix} u \\ d \end{pmatrix}$ is the two-flavour fermionic field and M is the superposition of the scalar σ and pseudo-scalar iso-triplet π as following $M = g_\sigma \sigma \mathbb{1} + i g_\pi \gamma^5 \tau_i \pi^i$. Here, g_σ and g_π are real constants, and τ_i are the Pauli matrices. The following transformation properties must hold for chiral invariance on $\mathcal{L}_{\text{int}}$

$$\psi_{\text{L/R}} \to U_{\text{L/R}} \psi_{\text{L/R}} \,, \qquad\qquad M \to U_{\text{L}} M U_{\text{R}}^{\dagger} \,, \tag{2.3}$$

where $U_{\text{L/R}}$ are the $\text{SU}(2)_{\text{L/R}}$ transformation matrices.

The kinetic terms for the self-conjugate σ and π fields are

$$\mathcal{L}_{\text{KE}} = \frac{1}{2} \partial_\mu \sigma \partial^\mu \sigma + \frac{1}{2} \partial_\mu \pi^i \partial^\mu \pi^i = \frac{1}{4} \text{Tr}\big(\partial_\mu \Sigma \partial^\mu \Sigma^{\dagger} \big) \,, \tag{2.4}$$

where in the last equality, we have set $g_\sigma = g_\pi$ due to chiral invariance, and used the following simplifying relation for $M = g_\pi \Sigma$:

$$\frac{1}{2} \text{Tr}(\Sigma \Sigma^{\dagger}) = \frac{1}{2} \text{Tr}\big([\sigma + i \gamma_5 \tau_i \pi^i][\sigma - i \gamma_5 \tau_i \pi^i] \big) = \sigma^2 + \pi^2 \,. \tag{2.5}$$

Thereby, a $\text{SU}(2)_{\text{L}} \times \text{SU}(2)_{\text{R}}$ symmetric LσM Lagrangian may be constructed in terms of Σ as

$$\mathcal{L}_\sigma = i \bar{\psi} \gamma^\mu \partial_\mu \psi + \frac{1}{4} \text{Tr}\big(\partial_\mu \Sigma \partial^\mu \Sigma^{\dagger} \big) - \frac{1}{4} m^2 \text{Tr}\big(\Sigma \Sigma^{\dagger} \big) - \frac{1}{16} \lambda \text{Tr}\big((\Sigma \Sigma^{\dagger})^2 \big) - g_\pi \bar{\psi} \Sigma \psi \,. \tag{2.6}$$

2.4 Technicolor Lagrangian & chiral symmetry breaking

A two-flavour UV-complete TC theory has been the primary focus of [28]. The theory was extended to three flavours in [29] and its cosmological implications have been investigated in [30]. While this thesis primarily focuses on developing the analysis for probing BSM parameter spaces, with the three-flavour-TC inspired low-scale EFT as our toy model, we still provide a brief overview of the UV-complete LσM-based theory below for the sake of completeness. The proper phenomenological investigation of the full parameter space of the high-scale QCD-like TC theory is left for future studies. After this introduction, we will construct the low-scale EFT. For the readers interested in the details of the original model, we refer to the papers mentioned above.

2.4.1 Technicolor Lagrangian

The fundamental TC Lagrangian, which bears a similar form the QCD one, may be written as [30]:

$$\mathcal{L}_{\rm TC} = -\frac{1}{4}T^{\eta}_{\mu\nu}T^{\mu\nu}_{\eta} + i\bar{Q}\gamma^{\mu}\left(\partial_{\mu} - \frac{i}{2}g_{\rm W}W^{A}_{\mu}\tau_{A} - \frac{i}{2}g_{\rm TC}A'^{n}_{\mu}\tau_{n}\right)Q - m_{\mathcal{Q}}\bar{Q}Q$$
$$+ i\bar{S}\gamma^{\mu}\left(\partial_{\mu} - \frac{i}{2}g_{1}B_{\mu} - \frac{i}{2}g_{\rm TC}A'^{n}_{\mu}\tau_{n}\right)S - m_{S}\bar{S}S \qquad (2.7)$$

where A'^{n}_{μ} represents the T-gluon gauge field, $T^{\eta}_{\mu\nu}$ is the corresponding field strength tensor, and S and Q are the SU($\rm N_{TC} = 3$) vector-like iso-singlet ($Y_{\rm W} = 1/2$) and iso-doublet ($Y_{\rm W} = 0$) T-quarks, respectively. Since the vector-like T-quarks' left- and right-handed components transform identically under the $\rm SU(2)_W$ symmetry group, mass terms are not disallowed in the symmetry unbroken phase, and so receive "natural" masses[1].

2.4.2 LσM Technicolor Lagrangian

We would now like to formulate the chirally symmetric UV-complete TC Lagrangian using the LσM. Assuming a three-flavour theory ($\rm N_f = 3$) with three TC charges ($\rm N_{TC} = 3$), the T-quarks and T-antiquarks form the $\rm SU(3)_{L/R}$ triplets

$$\mathcal{Q}_{\rm L,R} = \begin{pmatrix} U \\ D \\ S \end{pmatrix}_{\rm L,R}, \qquad \bar{\mathcal{Q}}_{\rm L,R} = \begin{pmatrix} \bar{U} & \bar{D} & \bar{S} \end{pmatrix}_{\rm L,R},$$

with the transformation properties

$$\mathcal{Q}_{\rm L} \to \left(1 + \frac{i}{2}\zeta_{a}\lambda_{a}\right)\mathcal{Q}_{\rm L}, \qquad \mathcal{Q}_{\rm R} \to \left(1 + \frac{i}{2}\xi_{a}\lambda_{a}\right)\mathcal{Q}_{\rm R}, \qquad (2.8)$$

where $\frac{\lambda_a}{2}$ are the group generators of $\rm SU(3)_L$ and $\rm SU(3)_R$.

In analogy to QCD, the TC spectrum consists of the following pseudo-scalar and scalar T-mesons (T-quark and T-antiquark pairs), respectively

$$\pi^{+}, \pi^{0}, \pi^{-}, \qquad K^{+}, K^{0}, \bar{K}^{0}, K^{-}, \qquad \eta, \eta',$$
$$a^{+}, a^{0}, a^{-}, \qquad H^{+}, H^{0}, \bar{H}^{0}, H^{-}, \qquad f, \sigma.$$

The first eight T-mesons in the top-row correspond to the expected eight pseudo-Nambu-Goldstone bosons from the chiral symmetry $\rm SU(3)_L \times SU(3)_R$ breaking into the T-flavour

[1] That is, they do not rely on the Higgs mechanism to receive mass, unlike the SM quarks.

$\mathrm{SU(3)_V}$ group. The realization of this will become apparent during the discussion of chiral symmetry breaking. Analogously to the two-flavour case, the above listed fields form a bi-fundamental representation of the $\mathrm{SU(3)_L \times SU(3)_R}$ group when placed into the multiplet $\Sigma = \frac{\lambda_a}{2}\sigma_a - i\frac{\lambda_a}{2}\pi_a$, where σ_a are the scalar fields and π_a are pseudo-scalar fields [29, 31]:

$$\begin{aligned}\Sigma =&\frac{1}{\sqrt{2}}\begin{pmatrix} \frac{1}{\sqrt{2}}a^0 + \frac{1}{\sqrt{6}}f + \frac{1}{\sqrt{3}}\sigma & a^+ & H^+ \\ a^- & -\frac{1}{\sqrt{2}}a^0 + \frac{1}{\sqrt{6}}f + \frac{1}{\sqrt{3}}\sigma & H^0 \\ H^- & \bar{H}^0 & -\sqrt{\frac{2}{3}}f + \frac{1}{\sqrt{3}}\sigma \end{pmatrix} \\ &- \frac{i}{\sqrt{2}}\begin{pmatrix} \frac{1}{\sqrt{2}}\pi^0 + \frac{1}{\sqrt{6}}\eta + \frac{1}{\sqrt{3}}\eta' & \pi^+ & K^+ \\ \pi^- & -\frac{1}{\sqrt{2}}\pi^0 + \frac{1}{\sqrt{6}}\eta + \frac{1}{\sqrt{3}}\eta' & K^0 \\ K^- & \bar{K}^0 & -\sqrt{\frac{2}{3}}\eta + \frac{1}{\sqrt{3}}\eta' \end{pmatrix},\end{aligned}$$

with the transformation property

$$\Sigma^i_\alpha \to \Sigma^i_\alpha + \frac{i}{2}\zeta_a\lambda^i_k\Sigma^k_\alpha - \frac{i}{2}\xi_a\lambda^\beta_\alpha\Sigma^i_\beta. \tag{2.9}$$

The UV-complete LσM TC Lagrangian worked out in [29] may now be written down as

$$\begin{aligned}\mathcal{L}_\sigma =&i\bar{\mathcal{Q}}\gamma^\mu\partial_\mu\mathcal{Q} + \partial_\mu\Sigma^\dagger\partial^\mu\Sigma + \mu^2\,\mathrm{Tr}\left(\Sigma\Sigma^\dagger\right) - \lambda_1\left(\mathrm{Tr}\left(\Sigma^\dagger\Sigma\right)\right)^2 - 3\lambda_2\,\mathrm{Tr}\left(\Sigma^\dagger\Sigma\Sigma^\dagger\Sigma\right) \\ &+ 2\sqrt{6}\Lambda_3\mathrm{Re}(\det\Sigma) - \sqrt{6}\kappa(\bar{\mathcal{Q}}_L\Sigma\mathcal{Q}_R + \bar{\mathcal{Q}}_R\Sigma^\dagger\mathcal{Q}_L).\end{aligned} \tag{2.10}$$

The first two terms are the kinetic terms, while the remaining belong to the potential. The last term consists of the T-quark-meson interactions, corresponding to the Yukawa interactions discussed in Sec. 2.3, from which a linear source term is formed when evaluating the T-quark vacuum expectation value. The presence of the this linear term (in Σ) makes it possible to generate a non-trivial VEV in the σ meson field through the minimization of the meson potential[2], breaking chiral symmetry explicitly. Knowing that only the σ field will receive a VEV (apart from the Higgs field during EWSB), we go ahead and simplify the last term in the Lagrangian

$$\begin{aligned}\mathcal{L}_\sigma =&i\bar{\mathcal{Q}}\gamma^\mu\partial_\mu\mathcal{Q} + \partial_\mu\Sigma^\dagger\partial^\mu\Sigma + \mu^2\,\mathrm{Tr}\left(\Sigma\Sigma^\dagger\right) - \lambda_1\left(\mathrm{Tr}\left(\Sigma^\dagger\Sigma\right)\right)^2 - 3\lambda_2\,\mathrm{Tr}\left(\Sigma^\dagger\Sigma\Sigma^\dagger\Sigma\right) \\ &+ 2\sqrt{6}\Lambda_3\mathrm{Re}(\det\Sigma) - u\theta,\end{aligned} \tag{2.11}$$

with

$$\theta = \kappa\langle 0|\bar{U}_LU_R + \bar{U}_RU_L + \bar{D}_LD_R + \bar{D}_RD_L + \bar{S}_LS_R + \bar{S}_RS_L|0\rangle. \tag{2.12}$$

As will become evident in the following section, the θ term is responsible for the masses acquired by the pseudo-Goldstone bosons of the chiral symmetry breaking.

[2]The linear term pushes the global minimum of the potential away from the origin.

2.4.3 Chiral symmetry breaking

Chiral symmetry is broken by giving σ a non-zero VEV $\langle\sigma\rangle = u$ in the LσM Lagrangian in Eq. (2.11). Keeping the other fields' VEVs at zero, we find the vacuum potential

$$\langle V\rangle_{\mathrm{C}} = -\frac{\mu^2}{2}u^2 + \left(\frac{\lambda_1}{4} + \frac{\lambda_2}{4}\right)u^4 - \frac{\Lambda_3}{3}u^3 + u\theta, \tag{2.13}$$

Critical points of the potential are found via:

$$\left.\frac{\mathrm{d}V}{\mathrm{d}\phi_i}\right|_{\langle\sigma\rangle=u} = 0. \tag{2.14}$$

where i runs over all fields. These are commonly referred to as the tadpole equations. The only expression that is not automatically satisfied is the derivative with respect to σ, constraining μ^2 in the following way

$$\mu^2 = (\lambda_1 + \lambda_2)u^2 - \Lambda_3 u + \frac{\theta}{u}. \tag{2.15}$$

We must further ensure that the critical point is a minimum, what we refer to as local stability in this paper. It is well known that a critical point of a multi-variable function can be classified as a minimum if its Hessian, evaluated at that critical point, is positive definite. Equivalently, the point is a minimum if all eigenvalues of the Hessian, that is the squared masses, are positive. In our case, this condition is satisfied by employing a parameter space inversion where Lagrangian parameters are traded for the (squared) masses, making the latter free parameters. It is important to note, however, that while positive definiteness ensures we are in a local minimum, it does not guarantee a global one. The condition for being in a global minimum is referred to as the vacuum stability condition and will be discussed in more detail in Sec. 2.6.

The emerging particle masses in the Chiral broken phase, referred to as mass scales here, are found by computing the 18×18 Hessian mass-squared matrix and evaluating it at the given VEV configuration, that is $M^2_{ij} = \frac{\partial^2 V}{\partial\phi_i\partial\phi_j}\big|_{\langle\sigma\rangle=u}$. In general, a change of basis to the mass eigenstates by diagonalizing the resulting Hessian is required, however, the structure of Σ has been already chosen a priori to give rise to a mass-diagonal mass form for the components of Σ. Four unique mass scales are found, two for the pseudo-scalar (PS) T-mesons, and two for the scalar (S) T-mesons

$$M^2_{\mathrm{PS1}(0)} \coloneqq M^2_{\pi(0)} = M^2_{K(0)} = M^2_{\eta(0)} = -\frac{\theta}{u}, \tag{2.16}$$

$$M^2_{\mathrm{PS2}(0)} \coloneqq M^2_{\eta'(0)} = 3\Lambda_3 u - \frac{\theta}{u}, \tag{2.17}$$

$$M^2_{\mathrm{S1}(0)} \coloneqq M^2_{a(0)} = M^2_{H(0)} = M^2_{f(0)} = 2\lambda_2 u^2 + 2\Lambda_3 u - \frac{\theta}{u}, \tag{2.18}$$

$$M^2_{\mathrm{S2}(0)} \coloneqq M^2_{\sigma(0)} = 2\big(\lambda_1 + \lambda_2\big)u^2 - \Lambda_3 u - \frac{\theta}{u}, \tag{2.19}$$

where the zeros in the notation emphasise the point that the above mass scales are different from the physical masses appearing after EWSB. In the expression for $M^2_{\mathrm{PS1(0)}}$, we see that the masses for the pseudo-Goldstone bosons of chiral symmetry breaking indeed arise from the explicit symmetry breaking term θ. The above relations can be inverted to express the remaining Lagrangian parameters $\theta, \lambda_1, \lambda_2, \Lambda_3$ in terms of the mass scales

$$\theta^{(\mathrm{h})} = -u\, M^2_{\mathrm{PS1(0)}} \tag{2.20}$$

$$\lambda_1^{(\mathrm{h})} = -\frac{1}{2u^2}(M^2_{\mathrm{PS1(0)}} - M^2_{\mathrm{PS2(0)}} + M^2_{\mathrm{S1(0)}} - M^2_{\mathrm{S2(0)}}) \tag{2.21}$$

$$\lambda_2^{(\mathrm{h})} = -\frac{1}{6u^2}(M^2_{\mathrm{PS1(0)}} + 2M^2_{\mathrm{PS2(0)}} - 3M^2_{\mathrm{S1(0)}}) \tag{2.22}$$

$$\Lambda_3^{(\mathrm{h})} = -\frac{1}{3u}(M^2_{\mathrm{PS1(0)}} - M^2_{\mathrm{PS2(0)}}) \tag{2.23}$$

where the (h) superscripts have been added to indicate that these are Lagrangian parameters belonging to the high-scale theory. After EWSB, the fields will receive unique physical masses, split around the original mass scales $M^2_{\mathrm{PS1(0)}}$, $M^2_{\mathrm{PS2(0)}}$, $M^2_{\mathrm{S1(0)}}$ and $M^2_{\mathrm{S2(0)}}$. The high-scale Lagrangian parameters $\theta^{(\mathrm{h})}$, $\lambda_1^{(\mathrm{h})}$, $\lambda_2^{(\mathrm{h})}$ and $\Lambda_3^{(\mathrm{h})}$ therefore give us control over which fields become relevant modes at lower scales, assuming the physical masses do not flow far away from their respective mass scales due to radiative corrections.

2.5 Low scale EFT limit and EW symmetry breaking

2.5.1 EW scale Technicolor Lagrangian

With the UV-limit TC introduction out of the way, we may now proceed to construct our toy model. The construction of the full EW-scale TC Lagrangian, which the toy model is based on, effectively amounts to extending the chirally symmetric LσM Lagrangian by incorporating chiral symmetry-violating interactions that still respect EW symmetry.

The $\mathrm{SU(2)_W} \times U(1)_Y$ invariants are formed by considering the following quantum numbers: The Higgs fields fall into the fundamental $\mathrm{SU(2)_W}$ representation

$$\mathcal{H} = \begin{pmatrix} H^+ \\ H^0 \end{pmatrix}, \qquad \mathcal{K} = \begin{pmatrix} K^+ \\ K^0 \end{pmatrix},$$

carrying hypercharge $Y_{\mathcal{H}} = Y_{\mathcal{K}} = 1/2$. The a and π fields transform under the adjoint representation, which can be represented by traceless 2x2 matrices

$$\pi = \begin{pmatrix} \frac{1}{\sqrt{2}}\pi^0 & \pi^- \\ \pi^+ & -\frac{1}{\sqrt{2}}\pi^0 \end{pmatrix}, \qquad a = \begin{pmatrix} \frac{1}{\sqrt{2}}a^0 & a^- \\ a^+ & -\frac{1}{\sqrt{2}}a^0 \end{pmatrix},$$

The triplets carry hypercharge $Y_\pi = Y_a = 0$. The remaining fields η, η', f and σ have zero hypercharge and are $\mathrm{SU(2)_W}$ singlets.

Recalling that we are able to create a hierarchy of physcial masses by using the relations between the high-scale Lagrangian parameters and the mass scales in Eqs. (2.20) to (2.23), we may reduce the number of relevant modes at the EW scale. We choose to do a case study of high-scale parameters θ^{h}, λ_1^{h}, λ_2^{h} and Λ_3^{h} that imply $M_{\mathrm{PS1}}^2 \ll M_{\mathrm{PS2}}^2, M_{\mathrm{S1}}^2, M_{\mathrm{S2}}^2$. Setting $M_{\mathrm{LS}}^2 \sim M_{\mathrm{PS1}}^2$ and $M_{\mathrm{HS}}^2 \sim M_{\mathrm{PS2}}^2, M_{\mathrm{S1}}^2, M_{\mathrm{S2}}^2$, this would entail the following

$$\theta^{(\mathrm{h})} \sim u\, M_{\mathrm{LS}}^2, \qquad \lambda_1^{(\mathrm{h})} \sim \frac{1}{2u^2}(M_{\mathrm{HS}}^2 - M_{\mathrm{LS}}^2), \tag{2.24}$$

$$\lambda_2^{(\mathrm{h})} \sim \frac{1}{6u^2}(M_{\mathrm{HS}}^2 - M_{\mathrm{LS}}^2), \qquad \Lambda_3^{(\mathrm{h})} \sim \frac{1}{3u}(M_{\mathrm{HS}}^2 - M_{\mathrm{LS}}^2). \tag{2.25}$$

The physical masses will be distributed around their respective mass scales up to RG effects. Assuming the RG effects to be small, only the fields associated with the first set of scalar T-mesons ($\mathcal{H}$, a, f) remain relevant degrees of freedom at the EW scale, while the remaining modes can safely be integrated out, resulting in our low-scale EFT limit

$$\begin{aligned} V_{\mathrm{LS}} =& \mu_{\mathrm{S}}^2 f^2 + \mu_{\mathrm{T}}^2 \mathrm{Tr}(aa) + \mu_{\mathrm{H}}^2 \mathcal{H}^\dagger \mathcal{H} + \\ & \Lambda_1 f^3 + \Lambda_2 f \mathrm{Tr}(aa) + \Lambda_3 f \mathcal{H}^\dagger \mathcal{H} + \Lambda_4 \mathcal{H}^\dagger a \mathcal{H} + \\ & \lambda_1 f^4 + \lambda_2 f^2 \mathrm{Tr}(aa) + \lambda_3 f^2 \mathcal{H}^\dagger \mathcal{H} + \lambda_4 f \mathcal{H}^\dagger a \mathcal{H} + \\ & \lambda_5 (\mathcal{H}^\dagger \mathcal{H})^2 + \lambda_6 \mathcal{H}^\dagger aa \mathcal{H} + \lambda_7 \mathrm{Tr}(aaaa), \end{aligned} \tag{2.26}$$

where we additionally require that μ_{H}^2 flows towards negative values due to the RG (while μ_{S}^2 and μ_{T}^2 are kept positive), causing the Higgs to spontaneously break EW symmetry. The assumption that the RG flow is small, allowing the physical masses to remain close to their original mass scales, while still driving μ_{H}^2 towards negative values, is a simplification done for convenience, albeit a crude one. This assumption does not explicitly enter our analysis, but is rather used to draw a connection between our toy model and the original UV-complete TC theory. To realize this assumption, one must compute the RG equations and select the appropriate parameters that result in the scenario outlined above. This is planned for future work. In our toy model, we will assume all couplings to be real.

This low-scale Lagrangian will be our primary focus in the development of the analysis and will be treated as a stand-alone theory. This amounts to treating the low-scale couplings independent from the high-scale ones, giving us (so far) 14 free couplings. In the original UV-complete Lagrangian Eq. (2.10), several interactions shared the same couplings. However, these couplings will have different RG flows when pushed down to the EW-scale and since RG equations are omitted here, we decide to treat the low-scale couplings in an independent manner in this first analysis. Information regarding the relation between the couplings is lost this way. A direct drawback is the increased dimensionality of the input space to the neural network, generally making training of the ANN more complicated. Before matching, V_{LS} may therefore be seen as a $\mathrm{SU}(2)_{\mathrm{W}}$ Singlet-Triplet Extended Standard Model (STESM) in which only the Higgs receives a VEV. The possibility of giving VEVs to the triplet and singlet in addition to the Higgs is discussed in Sec. 2.6.2. It should be

noted that although $V_{\rm LS}$ is treated as a toy model here, the STESM is still a phenomenologically interesting model despite its simplicity. In particular, there exist dark matter studies where the singlet and triplet are set to be charged under a $\mathbb{Z}_2$ symmetry [32].

2.5.2 Electroweak symmetry breaking

Similarly to the SM, EWSB is induced by supplying the H^0 with the non-zero vacuum expectation value $\langle H^0 \rangle = \frac{1}{\sqrt{2}} v$ with $v = 246$ GeV. Inserting the Higgs VEV into $V_{\rm LS}$, while keeping the other fields' VEVS at zero, gives us the following simple EW vacuum potential

$$\langle V_{\rm LS} \rangle = \frac{\mu_{\rm H}^2 v^2}{2} + \frac{\lambda_5 v^4}{4} \tag{2.27}$$

Out of the eight fields present in the low-scale Lagrangian, three yield non-trivial tadpole equations, giving us the constraints

$$\Lambda_3 = 0, \qquad \Lambda_4 = 0, \qquad \mu_{\rm H}^2 = -\lambda_5 v^2 \tag{2.28}$$

Interestingly, two of the interactions are disallowed by tadpole equations, even though they are allowed by symmetry. Considering the potential as a function of the $\mathcal{H}$, a and f field values, one can see that for certain non-zero Λ_3 and Λ_4, there will not exist any critical points along the vanishing expectation values $\langle a \rangle = \langle f \rangle = 0$. Instead, they are pushed along the a and f axes, but since we earlier assumed that the triplet and singlet fields do not acquire non-zero VEVs, we cannot "reach" any potential minima in that case. Therefore, interactions belonging to Λ_3 and Λ_4 are allowed by tadpole equations only if one in addition to the Higgs, allows for non-zero VEVs for the triplet and/or singlet.

The emerging particle masses after the EWSB are found by computing the 8×8 Hessian matrix. For later convenience, the procedure is performed in the complex weak basis: $M_{ij}^2 = \frac{\partial^2 V_{\rm LS}}{\partial \phi_i \partial \phi_j^\dagger}\big|_{\phi_i = \langle \phi_i \rangle, \phi_j = \langle \phi_j \rangle}$, where ϕ_i here are complex weak eigenstates of the fields. Below, the Hessian is separated for charged and neutral fields.

Starting with the charged states $a^\pm$ and $H^\pm$, their Hessian mass-squared matrix is automatically diagonal

$$M_{\rm C}^2 = \begin{pmatrix} 2\mu_T^2 + \frac{\lambda_6 v^2}{2} & 0 \\ 0 & 0 \end{pmatrix}, \tag{2.29}$$

giving us a charged massive and massless boson each

$$M_{\rm C}^2[1,1] = 2\mu_T^2 + \frac{\lambda_6 v^2}{2} \tag{2.30}$$

$$M_{\rm C}^2[2,2] = 0 \tag{2.31}$$

Considering the neutral fields a^0, H^0, $\bar{H}^0$ and f, their mass-squared matrix is

$$\tilde{M}^2_{\rm N} = \begin{pmatrix} 2\mu_T^2 + \frac{\lambda_6 v^2}{2} & 0 & 0 & -\frac{\lambda_4 v^2}{2\sqrt{2}} \\ 0 & \lambda_5 v^2 & \lambda_5 v^2 & 0 \\ 0 & \lambda_5 v^2 & \lambda_5 v^2 & 0 \\ -\frac{\lambda_4 v^2}{2\sqrt{2}} & 0 & 0 & 2\mu_S^2 + \lambda_3 v^2 \end{pmatrix}, \tag{2.32}$$

whose eigenvalues are

$$M^2_{\rm N}[1,1] = 0, \tag{2.33}$$

$$M^2_{\rm N}[2,2] = 2\lambda_5 v^2, \tag{2.34}$$

$$M^2_{\rm N}[3,3] = \mu_S^2 + \mu_T^2 + \frac{1}{4}(\lambda_6 + 2\lambda_3)v^2 - \sqrt{16(\mu_{\rm S}^2 - \mu_{\rm T}^2)^2 - 8(\lambda_6 - 2\lambda_3)(\mu_{\rm S}^2 - \mu_{\rm T}^2)v^2 + \left((\lambda_6 - 2\lambda_3)^2 + 2\lambda_4^2\right)v^4}\Big), \tag{2.35}$$

$$M^2_{\rm N}[4,4] = \mu_S^2 + \mu_T^2 + \frac{1}{4}(\lambda_6 + 2\lambda_3)v^2 + \sqrt{16(\mu_{\rm S}^2 - \mu_{\rm T}^2)^2 - 8(\lambda_6 - 2\lambda_3)(\mu_{\rm S}^2 - \mu_{\rm T}^2)v^2 + \left((\lambda_6 - 2\lambda_3)^2 + 2\lambda_4^2\right)v^4}\Big), \tag{2.36}$$

predicting a third massless boson, in addition to three massive neutrally charged scalars.

The three massless bosons found above correspond to the three EW Goldstone bosons of the SM and, similarly, they may be interpreted as the longitudinal polarizations of the vector bosons $W^\pm$ and Z. Additionally, $M^2_{\rm N}[2,2]$ should be associated with the SM Higgs boson and its experimentally observed mass.

2.6 Theoretical constraints

2.6.1 Local stability

As was discussed in Sec. 2.4.3, local stability is automatically satisfied by a non-imaginary mass spectrum. Therefore, to ensure local stability in our EW-scale theory, we use the relations (2.30) and (2.34)-(2.36) to trade four Lagrangian input parameters for the four unique (non-Goldstone) physical mass squares $M^2_{\rm C}[1,1]$, $M^2_{\rm N}[2,2]$, $M^2_{\rm N}[3,3]$ and $M^2_{\rm N}[4,4]$. From now on, these masses are denoted as $m_{\rm C}$, m_h, $m_{\rm N_1}$ and $m_{\rm N_2}$ respectively, with the

Higgs mass fixed at $m_h = 125.25$ GeV [6]. The inversion relation is

$$\lambda_4 = \frac{2^{3/2}}{v^2}\sqrt{m_{\rm C}^2 - m_{\rm N_1}^2}\sqrt{m_{\rm N_2}^2 - m_{\rm C}^2}\,, \tag{2.37}$$

$$\lambda_5 = \frac{m_h^2}{2v^2}\,, \tag{2.38}$$

$$\mu_{\rm T}^2 = \frac{1}{4}(2m_{\rm C}^2 - \lambda_6 v^2)\,, \tag{2.39}$$

$$\mu_{\rm S}^2 = \frac{1}{2}(m_{\rm N_1}^2 + m_{\rm N_2}^2 - m_{\rm C}^2 - \lambda_3 v^2)\,, \tag{2.40}$$

The λ_4 quartic coupling will only be real when $m_{\rm N_2}^2 > m_{\rm C}^2 > m_{\rm N_1}^2$ or $m_{\rm N_2}^2 < m_{\rm C}^2 < m_{\rm N_1}^2$. Additionally, we set $m_{\rm C}^2 > \frac{\lambda_6 v^2}{2}$ and $m_{\rm N_1}^2 + m_{\rm N_2}^2 > m_{\rm C}^2 + \lambda_3 v^2$ so that the triplet and singlet keep their positive mass terms.

To summarize, in the stand-alone STESM theory given by Eq. (2.26), there were initially 14 independent couplings. Three of these couplings (Λ_3, Λ_4 and $\mu_{\rm H}^2$) were fixed by solving the tadpole equations. Thereafter, by a simple inversion procedure, the four unique (non-Goldstone) masses ($m_{\rm C}$, $m_{\rm h}$, $m_{\rm N_1}$ and $m_{\rm N_2}$) were traded for four Lagrangian parameters (λ_4, λ_5, $\mu_{\rm T}^2$ and $\mu_{\rm S}^2$). One of these physical masses is the SM Higgs boson, and so is fixed at the measured Higgs mass. In the end, we are left with 10 degrees of freedom, namely Λ_1, Λ_2, λ_i, $m_{\rm C}$, $m_{\rm N_1}$ and $m_{\rm N_2}$ for $i = 1, 2, 3, 6, 7$, serving as input to our neural network.

2.6.2 Vacuum stability

Although we can locate a local minimum (along $\langle a\rangle = \langle f\rangle = 0$) using local stability, it does not guarantee that the minimum is a global one. Being in a global minimum ensures that there is no possibility for the system to quantum mechanically tunnel to a configuration with lower energy. In certain cases for the STESM theory however, the lower extremum is pushed along the a and f axes, making it impossible to reach the global minimum while respecting the initial $\langle a\rangle = \langle f\rangle = 0$ assumption. This leads us to the topic of vacua configuration, which involves assigning appropriate non-zero VEVs to the relevant fields to ensure the attainment of the global minimum. In this thesis however, our focus is primarily on establishing local stability. In future investigations, a more thorough exploration of the vacua configuration that leads to the global minimum will be warranted.

2.6.3 Boundedness from below

A prerequisite for the existence of a global minimum in the potential is that it remains bounded from below, meaning it does not tend to minus infinity in any arbitrary direction $|\mathbf{\Phi}| = |(\mathcal{H}, a, f)| \to \infty$ [33]. However, in the context of effective field theories, which are only defined up to certain matching scales, fields are restricted to finite values. In such

cases, the boundedness from below condition may be reinterpreted as the potential not taking on large negative values when the field values approach the matching scale in arbitrary directions.

Since quartic interactions dominate at large field values, their corresponding couplings are the most relevant. We impose the requirement that most quartic couplings belonging to interactions containing only bilinears must be positive, since these terms will then always have a positive contribution to the potential. We leave λ_4, whose interaction can take on both signs, and λ_6, as the only unconstrained quartic couplings. The latter, which consists of only bilinears, is left unconstrained to make it compatible with our collider constraints later (see Sec. 6.1). This set of constraints will not always yield a potential that is bounded from below (e.g., when $\lambda_4 f\mathcal{H}^\dagger a\mathcal{H}$ is negative and large in magnitude, while the remaining quartic couplings are close to zero), but will still overconstrain the parameter space in many cases. Given the highly approximate nature of these constraints, they are not intended to be used as part of the ANN training process. Instead, we will solely consider them at the end to assess if the obtained physical points approximately satisfy the boundedness from below condition.

2.6.4 Tree-level unitarity

Unitarity is a fundamental requirement that the scattering-matrix (S-matrix) must be unitary, meaning $SS^\dagger = \mathbb{1}$. The S-matrix allows for the computation of probabilities associated with the production of certain final states, given some initial states and scattering processes [34]. Naturally, the probabilities are required to be conserved. These constraints are typically expressed via the eigenvalues of the S-matrix. At tree-level, unitarity simply requires that the scattering matrix eigenvalues be smaller than the unitarity limit [13, 35].

2.7 Model implementation using `SARAH` and `SPheno`

The EW-scale STESM Lagrangian in Eq. (2.26) was implemented into the Mathematica package `SARAH-4.15.0` [14, 15, 16]. The model implementation mainly involves defining the fields' representations under $\mathrm{U}(1)_\mathrm{Y} \times \mathrm{SU}(2)_\mathrm{W} \times \mathrm{SU}(3)_\mathrm{C}$, defining the Lagrangian and specifying which fields mix. The TC gauge symmetry was not added to the model implementation since at the EW scale $\Lambda_\mathrm{EW} \sim \mathcal{O}(100\ \mathrm{GeV})$, the intrinsic structure of the TC bound states no longer remains prominent. The T-bound states may therefore be treated as fundamental particles. The implemented model was then exported to the `FORTRAN` package `SPheno-4.0.5` [20, 21]. Given numerical input for the Lagrangian parameters, `SPheno` was used to numerically compute the tree-level masses and tree-level unitarity constraints considering two-particle scattering.

3 Collider Constraints

3.1 Higgs physics

The Higgs sector plays a crucial role in addressing some of the limitations and challenges of the SM. To overcome those challenges, different extensions of the Higgs sector are routinely proposed. Therefore, constraining new theories via the Higgs sector by comparing predictions to experiments, becomes a valuable tool. As part of the framework developed in this thesis, constraints on Higgs physics are determined by comparing our model's prediction to current experimental exclusion limits on production and decay channels related to the predicted Higgs boson(s). For these limits, we apply the `FORTRAN` codes `HiggsBounds-5.10.2` [17, 18, 11] and `HiggsSignals-2.6.2` [19, 12].

Since many new theories contain enlarged Higgs sectors, often predicting multiple massive Higgs bosons, non-observation measurements play a crucial role in constraining parameter spaces. Using published data from LEP, the Tevatron and the LHC, `HiggsBounds` collects exclusion limits on the upper limits of cross-sections for specific "signal topologies" based on non-observation Higgs searches. A signal topology refers to a particular Higgs production and decay process, e.g. $e^+e^- \to h_i Z \to b\bar{b}Z$. The exclusion limits are expressed at 95% confidence level (C.L.). For data from the LEP, exclusion limits are mainly applied onto Higgsstrahlung ($e^+e^- \to hZ$) and double Higgs production ($e^+e^- \to hh$) processes with final decay states $\bar{b}b$ and $\tau^+\tau^-$. For the LHC and Tevatron, `HiggsBounds` considers gluon fusion ($gg \to h$), Higgsstrahlung ($q\bar{q}' \to hV$, $V = Z, W^\pm$), vector boson fusion ($qq' \to hq''q'''$) and Higgs production associated with heavy quarks ($gg \to t\bar{t}h, b\bar{b}h$) [11].

To assess the compatibility between theory and experiment for a given (negative) Higgs search, `HiggsBounds` computes the associated product of the cross-section (σ) and branching ratio (BR) denoted as $Q_{\text{obs}}(Y) = \sigma_{\text{obs}}(Y) \times \text{BR}(Y)$. Here, Y represents some signal topology from LEP, the Tevatron or the LHC. The upper limit of this product, dictated by the exclusion limits mentioned above, is denoted by $\bar{Q}_{\text{obs}}$. Thus, in the scenario of N Higgs bosons predicted by the theory, `HiggsBounds` selects the most statistically sensitive channel Y_i' for each boson, and requires that

$$\frac{Q_{\text{model}}(Y_i')}{\bar{Q}_{\text{obs}}(Y_i')} < 1, \tag{3.1}$$

for $i = 1, 2, ..., N$. Here, Q_{model} represents the cross-section branching ratio product predicted by the model under consideration. If Eq. (3.1) is not satisfied by all Higgs bosons in the model, it means a signal has been overestimated by the model, and the associated parameter space point can be excluded at 95% C.L.

`HiggsSignals` on the other hand, compares the signal strengths and masses of predicted peaks to the observed ones (i.e positive Higgs searches). The signal strength measure-

ments mainly correspond to Higgs decays to vector bosons ($h \to W^+W^- \to \ell^+\nu\ell'^-\nu'$, $h \to ZZ \to \ell^+\ell^-\ell'^+\ell'^-$), photons ($h \to \gamma\gamma$), tau leptons ($h \to \tau^+\tau^-$) and bottom quarks ($h \to b\bar{b}$) [36]. The package offers two complementary methods to estimate the compatibility, the peak-centered and mass-centered methods. In the peak-centered measure, the signal strength measurements predicted by the model and of published data is compared at the observed Higgs mass, while in the mass-centered method the rates are compared at the predicted Higgs mass(es). Both of these methods supply χ^2 estimates to quantify the level of agreement between the exotic Higgs sector predictions and collider experiment observations, which can be translated into a p-value. We set the p-value cut-off at $p = 0.05$.

Both `HiggsBounds` and `HiggsSignals` share similar inputs requirements. The inputs mainly consist of specifying the Higgs boson masses, Higgs branching ratios, Higgs total decay widths, as well as the couplings of the Higgs bosons to the SM fermions and bosons. The full list of inputs can be found at [18]. The Higgs boson properties (and others) required by the above packages can be computed by `SPheno`.

3.2 Oblique parameters

A convenient way of constraining electroweak radiative corrections of new physics is via the STU formalism of Peskin and Takeuchi. The formalism consists of three parameters S, T and U, which capture corrections to the gauge boson polarization functions. This type of correction is known as an oblique correction. Oblique corrections are only one of three types of EW radiative corrections, but dominate in the following scenario [9, 10]:

I The EW gauge group consists of $\mathrm{SU(2)_L} \times \mathrm{U(1)_Y}$ with the only associated gauge bosons being the photon γ and the weak bosons $W^\pm$ and Z.

II Coupling between new physics and light fermions is highly suppressed.

III The energy scale of the new physics M_{new} is large compared to the EW scale.

The above conditions are satisfied by the TC theory considered here. First, it leaves the electroweak group structure unchanged. Second, in our minimalistic approach, only the (TC) Higgs interacts with the SM sector, and identically to the SM Higgs boson, the exotic Higgs-SM interaction strength is proportional to the particle mass. Subsequently, the coupling between TC and the SM is small for light fermions. Finally, the new physics appears at $\mathcal{O}(1 - 100\ \text{TeV}) \gg \Lambda_{\text{EW}}$, satisfying the last criteria.

The STU parameters take on the following expressions [9]:

$$\alpha S = 4s_w^2 c_w^2 \left[\Pi'_{ZZ}(0) - \frac{c_w^2 - s_w^2}{s_w c_w} \Pi'_{Z\gamma}(0) - \Pi'_{\gamma\gamma}(0) \right], \tag{3.2a}$$

$$\alpha T = \frac{\Pi_{WW}(0)}{M_W^2} - \frac{\Pi_{ZZ}}{M_Z^2}, \tag{3.2b}$$

$$\alpha U = 4s_w^2 \left[\Pi'_{WW}(0) - c_w^2 \Pi'_{ZZ}(0) - 2 s_w c_w \Pi'_{Z\gamma}(0) - s_w^2 \Pi'_{\gamma\gamma}(0) \right], \tag{3.2c}$$

where α is the fine structure constant, $\Pi(q^2)$ is the vacuum polarization function, M_W and M_Z are the $W^\pm$ and Z boson masses, and s_w and c_w are the sine and cosine of the weak mixing angle.

The parameters are constructed in such a way that they are zero in the SM, and deviations in their values indicates new physics contributions. Generally, the U parameter will be comparably much smaller than S and T. We may therefore fix $U = 0$, yielding following S and T limits [6]:

$$S = -0.01 \pm 0.07, \tag{3.3a}$$

$$T = \ \ 0.04 \pm 0.06, \tag{3.3b}$$

at 68% C.L. A simultaneous fit of S and T (with $U = 0$) at 90% C.L. corresponds to the following set of points forming an ellipse on the ST-plane [37]

$$\mathcal{E}_{\mathrm{ST}} = \left\{ S, T \ \middle| \ \left(\frac{\tilde{S}\cos(\theta) + \tilde{T}\sin(\theta)}{a} \right)^2 + \left(\frac{\tilde{T}\cos(\theta) - \tilde{S}\sin(\theta)}{b} \right)^2 \leq 1 \right\}, \tag{3.4}$$

for $\tilde{S} = S$, $\tilde{T} = T - 0.05$, $\theta = 0.595$, $a = 0.1458$ and $b = 0.0437$. The computation of the oblique parameters is done by `SPheno`. The points are then be checked against the ellipse defined in Eq. (3.4).

4 Cosmic constraints

Cosmic phase transitions, the universe transitioning between two vacuum states driven by a change in the thermodynamic properties of the system, such as temperature, are of central interest in the study of cosmic implications of BSM theories. The phases are characterized by the symmetries that the space inside them respects. The type of transition between the phases can be classified into two categories; first- and second-order phase transitions. The transitions can be described by an order parameter, typically zero in the initial phase, and non-zero in the final phase [38].

If the transition between two ground states is a continuous one, that is, the order parameter is a well-behaved function of temperature (or some other thermodynamic observable), the transition is said to be of the second order. On the other hand, if the ground states co-exist at some temperature with a barrier separating them, the system must undergo Quantum-mechanical tunnelling from the local (metastable) minimum to the global (stable) minimum. This corresponds to the order parameter abruptly (discontinuously) changing value. Both scenarios have been plotted in Fig. 1 (left and middle). A point in the universe tunnelling between two minima can be seen as the formation (nucleation) of a bubble of the symmetry breaking phase, or "true vacuum", surrounded by the symmetry respecting phase, or "false vacuum". The bubbles, and therein the true vacuum, will continue to expand into the false vacuum, until the entire universe is filled with the symmetry broken phase. The bubble nucleation process is depicted in Fig. 1 (right). Here, we are disregarding strong supercooling effects, that is, the expansion of the universe slowing down the phase transition, and in some cases, even prohibiting it from completing. Hence, we work in the fast phase transition approximation [38, 39].

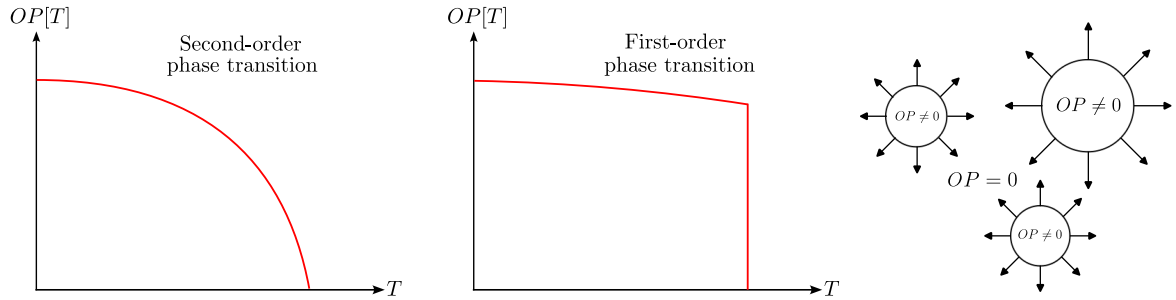

Figure 1: An illustration of the behaviour of the order parameter (OP) as a function of temperature T for second- (left) and first-order (middle) phase transitions. On the right, bubble nucleation (for a first-order phase transition) is demonstrated.

The objective of this section is two-fold. First, we will look into a formalism for describing the behaviour of quantum systems at finite temperature. For this task we use *dimensional reduction*, described in Sec. 4.1. Once the finite-temperature EFT is constructed, an investigation of its cosmic implications can be performed, covered in Sec. 4.2. The processes

discussed above source GWs, potentially detectable by future planned GW observatories such as LISA [40], DECIGO [41] and BBO [42]. The features we are interested in are strong FOPTs that produce GWs within the detecting capabilities of the GW observatories mentioned above.

4.1 Dimensional reduction

Dimensional reduction involves describing high-temperature effects with a purely bosonic 3D EFT, derived from the original 4D Lagrangian. This approach avoids the non-perturbative effects originating from massless vector bosons. Perturbation theory is still commonly used as an approximation though. However, it has been shown that it exhibits slow convergence and suffers from large theoretical uncertainties stemming from a strong dependence on the renormalization scale [43].

4.1.1 Superheavy, heavy and light modes

There are three energy scales which are of particular importance in dimensional reduction. For demonstration purposes, we look at a generic theory containing a gauge field A^μ, scalar field ϕ and a fermionic field ψ. Its Lagrangian is

$$\mathcal{L} = -\frac{1}{4}F^{\mu\nu}F_{\mu\nu} + (D^\mu\phi)^\dagger(D_\mu\phi) + \bar{\psi}\gamma^\mu D_\mu\psi - V(\phi) - g_{\mathrm{Y}}\bar{\psi}\phi\psi + \delta\mathcal{L}, \tag{4.1}$$

where g_{Y} and λ are the Yukawa and scalar couplings, respectively, $F^{\mu\nu}$ is the field-strength tensor, D_μ is the covariant derivative, $V(\phi)$ is the scalar field potential

$$V(\phi) = m_S^2\phi^\dagger\phi + \lambda\big(\phi^\dagger\phi\big)^2 \tag{4.2}$$

and $\delta\mathcal{L}$ are the counterterms. The bosons and fermions are the Matsubara fields

$$\phi(x,\tau) = \sum_{n=-\infty}^{\infty} \phi_n(x)\exp\big(i\omega_n^b\tau\big), \tag{4.3}$$

$$\psi(x,\tau) = \sum_{n=-\infty}^{\infty} \psi_n(x)\exp\big(i\omega_n^f\tau\big), \tag{4.4}$$

where τ is the imaginary time variable. The discrete frequencies $\omega_n^b = 2n\pi T$ and $\omega_n^f = (2n+1)\pi T$ can be interpreted as the 3D tree-level masses for the bosonic and fermionic modes respectively

The magnitude of the bosonic and fermionic masses after thermal corrections lie in three scales: the superheavy $\sim \pi T$, heavy $\sim gT$ and light $\sim g^2T$ scales, with g as the gauge coupling of the theory. The 3D masses of the non-static ($n \neq 0$) bosonic and all (any n)

fermionic modes lie in the πT scale, i.e are superheavy. For the static bosonic mode, the effective mass after one-loop thermal corrections can generally be written as [43]:

$$m_{\text{eff}}^2(T) = \gamma T^2 + m_{\text{tree}}^2, \tag{4.5}$$

with $\gamma \sim g^2$. Obviously gauge fields have $m_{\text{tree}}^2 = 0$, but the temporal components get a non-zero correction $\gamma \neq 0$. Hence, the spatial A^i and temporal A^0 gauge components are light and heavy respectively at one-loop level. The scalar fields are heavy if $m_{\text{tree}}^2 \neq -\gamma T^2$ ($\Rightarrow m_{\text{eff}}^2 \sim (gT)^2$), or light if $m_{\text{tree}}^2 \sim -\gamma T^2$ ($\Rightarrow m_{\text{eff}}^2 \sim (g^2 T)$).

4.1.2 Three-dimensional effective field theories

There are two levels of dimensional reduction. In the first, the EFT is a theory of heavy and light modes, with the superheavy modes integrated out. In the second, only light modes are kept [43].

Removing all superheavy modes from Eq. (4.1), we get the 3D EFT of heavy and light modes

$$\mathcal{L} = -\frac{1}{4}F^{ij}F_{ij} + \big(D^i\phi\big)^\dagger(D_i\phi) + \frac{1}{2}(D^iA_0)(D_iA^0) - V_3(\phi, A^0) + \delta\mathcal{L}, \tag{4.6}$$

with

$$V_3(\phi, A_0) = m^2\phi^\dagger\phi + \lambda_3\big(\phi^\dagger\phi\big)^2 + h_3\phi^\dagger\phi A_0^2 + \frac{1}{2}m_{\text{D}}^2A_0^2 + \frac{1}{4}\lambda_A A_0^4. \tag{4.7}$$

Here, g_3 is the gauge coupling with dimension $\text{GeV}^{1/2}$, λ_3 is a scalar coupling with dimension GeV and the temporal gauge component A_0 has received a mass term $m_{\text{D}} \sim gT$. Since all modes in the range of πT have been integrated out, this EFT is only valid up to momenta $k \sim gT$. We additionally require $k \ll T$ for the dimensional reduction to remain valid.

Further removing all heavy modes, we get the 3D EFT of only the light modes

$$\mathcal{L} = -\frac{1}{4}F^{ij}F_{ij} + \big(D^i\phi\big)^\dagger(D_i\phi) - V_3(\phi) + \delta\mathcal{L}, \tag{4.8}$$

with

$$V_3(\phi) = m_3^2\phi^\dagger\phi + \bar{\lambda}_3\big(\phi^\dagger\phi\big)^2, \tag{4.9}$$

where only the light scalar fields ($m_{\text{tree}}^2 \sim -\gamma T^2$) should be included.

4.1.3 Matching

Dimensional reduction simply requires us to write down the most general 3D Lagrangian containing the relevant fields and fixing the 3D theory couplings by matching the 2-, 3- and

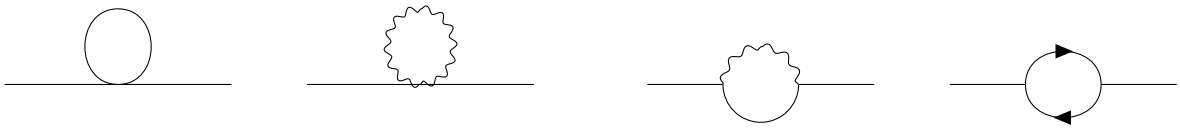

Figure 2: Examples of Feynman diagrams contributing to mass coupling corrections via the 2-point correlation function. The scalar field is denoted by a black line, fermionic field by a directed black line and the gauge field by a wiggly line.

4-point Green's functions of the 3D and underlying 4D theories. To match the dimensions between the n-point Green's functions, the 3D correlation function should be scaled by $T^{\frac{n}{2}-1}$ [43]. As an example, consider the 2-point correlation function

$$\left(\delta_{\mathrm{CT}} + m_S^2 + \Pi(k^2)\right)_{\mathrm{4D}} = \left(\delta_{3,\mathrm{CT}} + m_3^2\right)_{\mathrm{3D}}, \tag{4.10}$$

where $\Pi(k^2)$ is the self-energy, containing all diagrams that contribute to the 2-point correlation function. The δ_{CT} are counter terms to cancel divergences from the loop diagrams. For our simple Lagrangian in Eq. (4.1), examples of diagrams contributing to the 2-point correction are depicted in Fig. 2. Once the self-energy has been found, the 3D mass coupling m_3^2 can be found in terms of the equivalent 4D coupling m_S^2. Similarly, the 3- and 4-point correlation functions fix the cubic and quartic couplings of the 3D theory. These techniques are applied using the `Mathematica` package `DRalgo-1.0.2` [23], allowing us to calculate thermal masses at two-loop level and resummation of couplings at one-loop level. For more details on `DRalgo`$'s$ implementation of dimensional reduction, we refer the reader to the manual [23].

4.1.4 Beta functions

The beta functions, also computed by `DRalgo`, capture the effects of the thermal RG flows of the couplings and are defined as the differential with respect to the log of the RG-scale $\bar{\mu}$, with $\bar{\mu} = \pi T$. The beta functions for the 4D theory can be obtained by imposing the condition that the renormalized 4D couplings remain independent of $\bar{\mu}$, which implies that their beta functions vanish. Once expressions for the beta functions are found, they provide insight on the relevance of the associated operator (interaction) at different temperatures. In the case where an operator is deemed irrelevant at a certain temperate, that interaction may be omitted from that finite-temperature EFT [44].

4.2 Gravitational waves

We now turn to the investigation of the GW signature of the finite-temperature EFT. First, we cover some quantities relevant for GW computations, including the three-dimension Euclidean action, the phase transition energy budget and the phase transition (inverse) duration.

4.2.1 Euclidean action

The three-dimensional Euclidean action S_3 makes its first appearance in the decay rate of the false vacuum as a function of time t, defined as

$$\Gamma(t) = A(t) \exp\left(-S_3(t)/T\right), \tag{4.11}$$

where S_3 and the pre-factor A are given by

$$S_3(T) = 4\pi \int_0^\infty \mathrm{d}r\, r^2 \left(\frac{1}{2} \left(\frac{\mathrm{d}\phi}{\mathrm{d}r} \right)^2 + V_{\text{eff}}(\phi, T) \right), \tag{4.12}$$

$$A(T) = T^4 \left(\frac{S_3(T)}{2\pi T} \right)^{3/2}, \tag{4.13}$$

with r as the spherical radial coordinate and V_{eff} is the finite-temperature EFT [39]. Here, the effective potential is assumed to be four-dimensional. However, the finite-temperature EFT from dimensional reduction lives in three dimensions and can be related to the four-dimensional one by $V_{\text{eff}}(\phi, T) = T \cdot V_{\text{eff}}^{\text{3D}}(\phi/\sqrt{T})$ [45]. The expression for $\phi(r)$ can be found by solving the equation of motion

$$\frac{\mathrm{d}^2\phi(r)}{\mathrm{d}r^2} + \frac{2}{r}\frac{\mathrm{d}\phi(r)}{\mathrm{d}r} = \frac{\partial V_{\text{eff}}}{\partial \phi}. \tag{4.14}$$

The boundary conditions require false vacuum outside of the bubble $\phi(r) \overset{r\to\infty}{=} \phi_{\text{F}}$ and a non-singular origin $\frac{\mathrm{d}\phi(r)}{\mathrm{d}r}\big|_{r=0} = 0$. The solution to Eq. (4.14) is commonly referred to as the bounce solution [22, 39].

The reader should observe that time t and temperature T variables were used interchangeably in Eq. (4.11)-(4.13). This is due to the relation derived in [46]

$$\frac{\mathrm{d}T}{\mathrm{d}t} = -H(T)T, \tag{4.15}$$

where the Hubble parameter $H(T)$ is defined by

$$H(T) = \frac{T^2}{1.66\sqrt{g_*}} M_{\text{Pl}} \tag{4.16}$$

Above, the Planck mass is $M_{\text{Pl}} = 1.2 \times 10^{19}$ GeV and the relativistic degrees of freedom g_*, found by considering the relevant bosonic and fermionic degrees of freedom at a given temperature, will be treated as a constant $g_* = 106.75$ [47].

Some useful temperature classifications relevant to first-order phase transitions are the critical, nucleation and percolation temperatures. The critical temperature T_c is defined as the temperature at which the two minima (phases) co-exist and are degenerate, meaning

$$V_\mathrm{eff}(\phi = \phi_\mathrm{F}, T_\mathrm{c}) = V_\mathrm{eff}(\phi = \phi_\mathrm{T}, T_\mathrm{c}). \tag{4.17}$$

Secondly we have the nucleation temperature T_n. It is the temperature at which on average one bubble is nucleated per Hubble volume

$$N(T_\mathrm{n}) = \int_{t_\mathrm{c}}^{t_\mathrm{n}} \frac{\Gamma(t)}{H(t)^3}\, \mathrm{d}t = 1, \tag{4.18}$$

where $t_\mathrm{n/c}$ is the time at which $T = T_\mathrm{n/c}$. Lastly, the percolation temperature T_p is reached when 34% of the (false vacuum) space is converted to the true vacuum. Their magnitudes are related by $T_\mathrm{p} \leq T_\mathrm{n} \leq T_\mathrm{c}$ [39].

An approximate expression for the three-dimensional action can be found by inserting the expressions for the decay rate Eq. (4.11) and Hubble parameter Eq. (4.16) into Eq. (4.18), and making a Taylor expansion of $S_3(T)$ near T_n. Evaluating the integral leads to [48]

$$\left.\frac{S_3(T)}{T}\right|_{T_\mathrm{n}} \simeq 141.4 - 4\log\left(\frac{T_\mathrm{n}}{100\ \mathrm{GeV}}\right) - \log\left(\frac{\beta(T_\mathrm{n})}{100}\right). \tag{4.19}$$

For electroweak phase transitions, the last two terms are typically approximated away and the expression $S_3(T_\mathrm{n})/T_\mathrm{n} \simeq 140$ is used to identify the nucleation temperature of the system.

4.2.2 Energy budget

We will now take the first step in connecting the properties of the GW spectrum to the finite-temperature potential. The energy budget of the phase transition (the energy released) is described by the α parameter. It is therefore intuitive to also use α as a measure of the strength of the phase transition. We may express it as

$$\alpha_\theta = \left.\frac{3}{4}\frac{\theta_+ - \theta_-}{a_+ T^4}\right|_{T=T_p}, \tag{4.20}$$

where $\theta = (e - 3p)/4$ is the trace of the energy-momentum tensor, $e = V_\mathrm{eff} - T\ \partial V_\mathrm{eff}/\partial T$ is the energy density, $p = -V_\mathrm{eff}$ is the pressure and $a_+ = \pi^2 g_*/30$. The parameters θ_+ and θ_- should be evaluated in the true and false vacuums, respectively. The α parameter may therefore be simplified to

$$\alpha_\theta = \left.\frac{30}{\pi^2 g_\mathrm{eff} T^4}\left(\Delta V_\mathrm{eff} - \frac{T}{4}\frac{\partial \Delta V_\mathrm{eff}}{\partial T}\right)\right|_{T=T_\mathrm{p}} = \left.\frac{1}{\rho_\mathrm{rad}}\left(\rho_\mathrm{vac} - \frac{T}{4}\frac{\partial \rho_\mathrm{vac}}{\partial T}\right)\right|_{T=T_\mathrm{p}}, \tag{4.21}$$

where $\rho_{\rm rad}$ and $\rho_{\rm vac}$ are the vacuum and radiation energy densities, respectively, given by

$$\rho_{\rm rad} = g_* \frac{\pi^2}{30} T^4 \,, \tag{4.22}$$

$$\rho_{\rm vac} = \Delta V_{\rm eff}(\phi, T) \equiv V_{\rm eff}(\phi = \phi_{\rm T}, T) - V_{\rm eff}(\phi = \phi_{\rm F}, T) \,, \tag{4.23}$$

and the field value in the true/false vacuum is denoted by $\phi_{\rm T/F}$ [39]. In the radiation dominated epoch, another way to parameterize the strength of the phase transition is by the ratio $(\phi_{\rm T} - \phi_{\rm F})/T_{\rm c}$ [49]. The strong FOPT criteria is established by requiring $(\phi_{\rm T} - \phi_{\rm F})/T_{\rm c} > 1$ in our analysis.

4.2.3 Mean bubble separation

For fast phase transitions, the false vacuum decay rate may be approximated as [39]

$$\Gamma \approx \Gamma(t_0) \exp(\beta(t - t_0)), \tag{4.24}$$

where t_0 is typically set to the percolation time $t_{\rm p}$ and β may be interpreted as the inverse duration of the phase transition. The latter is approximated by [49]

$$\beta = -\frac{\mathrm{d}}{\mathrm{d}t} \frac{S_3(T)}{T} \bigg|_{t=t_0} = H(T) T \, \frac{\mathrm{d}}{\mathrm{d}T} \left(\frac{S_3(T)}{T} \right) \bigg|_{T=T_p} . \tag{4.25}$$

In the second equality the time-temperature relation was applied. The averaged nucleation rate is found in terms of the false vacuum probability $P(t)$ via

$$\begin{aligned} \bar{\Gamma}(t) =& P(t)\Gamma(t) = \\ =& \Gamma(t_0) \exp\left(\beta(t - t_0)\right) \, \exp\left(-I_0 \exp(\beta(t - t_0))\right), \end{aligned} \tag{4.26}$$

with $I_0 = 8\pi v_w^3 \Gamma(t_0) \beta^{-4}$ and v_w denoting the bubble wall speed. The second equality is explicitly shown in [39]. We work under the the non-runaway bubble assumption, where the expanding bubbles in the plasma reach a relativistic terminal velocity due to friction against the plasma. We pick $v_w = 0.95$, as such high speeds provide better possibilities for producing detectable GWs [49].

Finally, the mean bubble separation at time t is defined by

$$R(t) = (n_B(t))^{-1/3}, \tag{4.27}$$

$$n_{\rm B}(t) = \int_{t_c}^{t} \left(\frac{a(t')}{a(t)} \right)^3 \bar{\Gamma}(t') \, \mathrm{d}t', \tag{4.28}$$

where $n_{\rm B}(t)$ is the density of the bubbles and $a(t)$ is the scale factor of the Friedmann-Robertson-Walker metric. Inserting our expression for the averaged decay rate and evaluating the integral, one gets

$$n_{\rm B}(t) = \frac{\beta^3}{8\pi v_w^3} (1 - P(t)). \tag{4.29}$$

In the fast phase transition approximation, we may assume $P(t > t_{\rm p}) \simeq 0$ since the probability of finding the false vacuum becomes small. Hence, at $t = t_{\rm p}$, the mean bubble separation is found to be

$$R = \frac{(8\pi)^{1/3} v_w}{\beta}, \tag{4.30}$$

Observe that the mean bubble separation R is inversely proportional to the inverse duration of the phase transition β. These two parameters are therefore used interchangeably [39].

The evaluation of the bounce solution, and the computation of the nucleation temperature, phase transition duration β, energy budget α and other relevant quantities is performed by the `CosmoTransitions-2.0.6` package [22].

4.2.4 Gravitational-wave signature

During FOPTs, GWs are produced by three primary sources: the collisions of bubble walls, sound-waves generated by bubble collisions and Magnetohydrodynamic (MHD) turbulence in the plasma afterwards. Under the linearized approximation, the total spectrum of GWs from FOPTs is written as [39]:

$$h^2\Omega = h^2\Omega_{\rm coll} + h^2\Omega_{\rm sw} + h^2\Omega_{\rm turb}, \tag{4.31}$$

with the dimensionless Hubble parameter defined as $h = H_0/(100\ \text{km/s/Mpc})$ and Ω denoting the (dimensionless) GW amplitude. In the non-runaway bubble scenario, most of the energy budget α is converted to GWs from sound-waves and/or MHD turbulence. Generally, it is believed the MHD turbulence only has a small contribution to the GW spectrum when compared to sound-waves [39, 50]. In this thesis, we therefore approximate away GWs produced by MHD turbulence and solely focus on sound-waves.

The GW spectrum from the sound-waves has the form [39]

$$h^2\Omega_{\rm sw} = h^2\Omega_{\rm sw}^{\rm peak}\left(\frac{f}{f_{\rm sw}^{\rm peak}}\right)^3\left[\frac{4}{7} + \frac{3}{7}\left(\frac{f}{f_{\rm SW}^{\rm peak}}\right)^2\right]^{-\frac{7}{2}}. \tag{4.32}$$

Its peak amplitude $\Omega_{\rm sw}^{\rm peak}$ and associated peak frequency $f_{\rm sw}^{\rm peak}$ are given by

$$f_{\rm sw}^{\rm peak} \approx 1.9 \cdot 10^{-5}\ \text{Hz}\ \left(\frac{g_*}{100}\right)^{\frac{1}{6}}\left(\frac{T_{\rm reh}}{100\text{GeV}}\right)\left(\frac{(8\pi)^{\frac{1}{3}}}{H(T_{\rm p})R}\right), \tag{4.33}$$

$$h^2\Omega_{\rm sw}^{\rm peak} \approx 2.65 \cdot 10^{-6}\left(\frac{H(T_{\rm p})R}{(8\pi)^{\frac{1}{3}}}\right)\left(\frac{\kappa_{\rm sw}\alpha}{1+\alpha}\right)^2\left(\frac{100}{g_*}\right)^{\frac{1}{3}}. \tag{4.34}$$

Above, $T_{\rm reh}$ is known as the reheating temperature, given by

$$T_{\rm reh} \simeq T_{\rm p}(1+\alpha)^{1/4}, \tag{4.35}$$

and $\kappa_{\rm sw} = \sqrt{H(T_{\rm p})\tau_{\rm sw}}$ is an efficiency factor describing the ratio of the energy budget α that is transferred to the strength of the GWs produced by sound-waves, with $\tau_{\rm sw}$ being the length of the sound-wave period. It is found via

$$\tau_{\rm sw} = \min\left[\frac{1}{H(T_{\rm p})}, \frac{R_*}{\bar{U}_f}\right], \tag{4.36}$$

where $\bar{U}_f$ is the fluid velocity of the plasma, which under the high $v_{\rm w}$ limit is

$$\bar{U}_f^2 \simeq \frac{3}{4}\frac{\alpha}{1+\alpha}k_v. \tag{4.37}$$

with the k_v efficiency factor [39]:

$$k_v = \frac{\alpha}{0.73 + 083\sqrt{\alpha} + \alpha}. \tag{4.38}$$

It is important for the reader to note that some approximations employed here become increasingly inaccurate as phase transitions start approaching the supercooling regime, particularly Eqs. (4.19) and (4.24). Strong supercooling is typically associated with stronger FOPTs, and thereby larger energy budgets α [39]. To minimize these inaccuracies, one can introduce a cut-off for α. However, in this initial study, we keep points producing FOPTs with large energy budgets for the sake of gathering statistics.

4.2.5 Signal-to-noise-ratio

While certain points might produce GWs within the sensitivity curves of the GW observatories, the better measure of detectability of a GW signal is its signal-to-noise-ratio (SNR). The SNR depends on the detector configuration, computed via the observation time $\mathcal{T}$, the detector sensitivity curve $h^2\Omega_{\rm det}$ for a given configuration and the GW spectrum $h^2\Omega_{\rm GW}$ as following [49]

$$\text{SNR} = \sqrt{\mathcal{T}\int_{\rm f_{min}}^{f_{max}} \left(\frac{h^2\Omega_{\rm GW}(f)}{h^2\Omega_{\rm det}(f)}\right)^2}, \tag{4.39}$$

where the integration is over the frequency detection region of the detector.

5 Program structure

The framework for scanning parameter spaces against collider and GW measurement constraints is written in `Python-3.10.6`. The developed framework mainly consists of the following files; `Hub`, `DataConstructor`, `Network`, `UserInput` and a number of bash scripts (e.g. to run the HEP packages). Since our analysis relies on `SPheno` for unitarity and EW precision constraints, `HiggsBounds` and `HiggsSignals` for Higgs exclusion limits and `CosmoTransitions` for the order and strength of the phase transitions, these packages must be available. The GW peak amplitude and associated frequency, used to evaluate the detectability constraint in this thesis, are computed using code provided by António Morais. The BSM theory implementation is done in `SARAH`, which can then be used to export the model to `SPheno`. The implementation is straightforward and requires the definition of any new global or gauge symmetries, the Lagrangian, (non-SM) fields and their mixing. The finite-temperature EFT construction is done via `DRalgo`, requiring a similar implementation of the BSM theory as for `SARAH`. For its export to `CosmoTransitions`, a script provided by Mårten Bertenstam [51] was used. Since the framework is not made publicly available yet, as more development and testing is needed, only a selection of its key features will be highlighted in this section.

To use the framework, some input is required in `UserInput`, including paths to the HEP packages, ANN hyperparameter definitions[3], the parameter space definition (i.e ranges for the free parameters) and the number of points to scan. If the free parameters are different from the Lagrangian parameters (via some inversion procedure, e.g. particle masses traded for some Lagrangian parameters), this can be specified by including expressions relating the free and Lagrangian parameters in question. These definitions are needed to perform the analysis in `DataConstructor` and to define and train the ANN in `Network`. The ANN model is defined using the `TensorFlow-2.12.0` [52] `Python` library.

The main file to call to gather data, train the ANN or to make predictions with a trained ANN is `Hub`. Some of its settings and what they do are listed below:

1. If collider or cosmic training data construction is turned on, the parameter space is sampled using Sobol sequences[4] and passed to `DataConstructor`. The relevant HEP packages are called, with the data and results stored into training data files.

2. Since some constraints take much longer to check than others, the framework computes the latter first. An option is added so that the framework only checks the next constraint if it has satisfied all before it.

[3] In machine learning, the parameters controlling various aspects of the network structure and training are conventionally referred to as hyperparameters.

[4] Sobol sequences are low-discrepancy sequences, resulting in faster convergence than random sampling.

3. If network training is turned on, an ANN model is defined and trained using the data stored in the training data files. A summary with relevant plots of the training are printed, and the model details (architecture, weights) are saved for future use.

4. Turning on network predictions, a second (larger) parameter space sampling is performed and handed to the saved ANN. The trained neural network will suggest what it believes to be positive points (points satisfying all constraints). The suggested points are passed back to `DataConstructor` to analyze using the HEP packages, and the true positive points are stored and plotted.

In the upcoming section, we present a demonstration of our framework using a simple architecture for the ANN. Details about the model have been listed below. Although these details are not essential for interpreting the results, we will attempt to include explanations alongside the details when needed. For cases when the provided explanations are not sufficient, we refer the reader to [53].

We are addressing a binary classification problem here, where points are categorized as either positive or negative, and the objective of the network is to distinguish between them. Points in the training data files that satisfy all constraints simultaneously are assigned the positive label, while remaining points are labelled negative.

The architecture of the ANN is as follows: the input layer size corresponds to the number of free parameters, which in our case is ten (Λ_1, Λ_2, λ_i, m_{C}, m_{N_1}, m_{N_2} for $i = 1, 2, 3, 6, 7$). We employ six hidden layers, with 60 hidden nodes each, while the output layer consists of a single node. Given that this is a binary classification problem, the activation functions for the hidden nodes and the single output node are the rectified linear unit and the sigmoid function, respectively. The output of the sigmoid function (and thereby of the ANN) lies between 0 and 1, and should be interpreted as the probability that a certain point belongs to the positive class. Points with an output equal to or greater than 0.5 are predicted to be positive. We used the common choice of Adam as optimizer for our problem. We apply the L1 and L2 regularization techniques in each layer to prevent the ANN from overtraining on the training data.

Due to the observed strong imbalance between positive and negative points[5], some of this imbalance was addressed by undersampling the majority class before training the network. This way, we reduce the risk of the ANN solely focusing on the majority class[6]. Some class imbalance (1:100 in favour of negative points), combined with class weights (2:1 in favour of positive points) was found to be optimal for the ANN training however. Class

[5]There are far fewer points satisfying the constraints than the opposite.

[6]If there is a significant imbalance between the classes, the neural network might predict that all points belong to the majority class in order to maximize its accuracy. However, this would defeat the purpose of the ANN.

weights are used to assign greater emphasis to certain classes (the class of positive points in our case). This allows us to counter-act some of the remaining class imbalance without sacrificing more points (information) through undersampling. Oversampling the minority class was not observed to increase the performance of the ANN, and was therefore not considered.

6 Results

Before discussing the results, let us recap which constraints will be applied in our demonstration of the framework on the STESM. We consider theoretical and collider constraints, including unitarity, EW precision tests and Higgs exclusion limits. On the cosmic side, we require the presence of a FOPT, specifically a strong FOPT characterized by $(\phi_{\mathrm{T}}-\phi_{\mathrm{F}})/T_{\mathrm{c}} > 1$. In terms of detectability, for the sake of gathering statistics, we only set a constraint on the GW peak amplitude during ANN training, without specifying its associated frequency. Therefore, our detectability constraint is that the peak amplitude should be of similar magnitude to where the LISA, DECIGO and BBO sensitivity curves lie, around $h^2\Omega^{\mathrm{peak}} \sim 10^{-15}$.

Due to the expected scarcity of points satisfying all constraints, an initial investigation over a large region of parameter space, spanned by the free parameters Λ_1, Λ_2, λ_1, λ_2, λ_3, λ_6, λ_7, m_{N_1}, m_{N_2} and m_{C}, is performed. Once we have an understanding of how the constraints individually limit the parameter space, we will shift our focus to the region of interest, that is the region where points are more likely to satisfy all constraints simultaneously. Training data is collected inside the region of interest and the ANN is trained on the gathered data. The trained ANN will then be used to suggest positive points to us, which will be analyzed using the HEP packages, from which all true positive points can be collected. Although not the prime focus of the ANN training, we will plot the GW peak amplitudes $h^2\Omega^{\mathrm{peak}}$ against the associated peak frequencies f^{peak} for the positive points, along with the LISA, DECIGO and BBO sensitivity curves.

6.1 Initial scan

For the initial scan, we run it over the parameter space defined by the following free parameters

$$|\Lambda_i| < 5000 \text{ GeV}\,, \qquad |\lambda_j| < 15\,, \qquad 200 \text{ GeV} < m_k < 1000 \text{ GeV}\,,$$

for $i = 1, 2$, $j = 1, 2, 3, 6, 7$ and $k = \mathrm{N}_1, \mathrm{N}_2, \mathrm{C}$. Starting with theoretical and collider constraints, approximately 56 000 points in the above parameter space were investigated. Out of these, 90 points individually satisfying unitarity (U), Higgs exclusion limits (H) and oblique parameter constraints (STU) were randomly selected, and their Probability Density Functions (PDFs) estimated using kernel density estimation (KDE) in Fig. 3. The KDE is provided by the `Python` library `Seaborn` [54]. Since certain free parameter combinations give complex couplings via the tadpole equations, or negative μ_{S}^2 or μ_{T}^2 via the parameter space inversion procedure, with such points being discarded, the parameter space becomes non-uniformly sampled. Therefore, the background (BG) sampling distribution has been included in the plots to more easily identify any potential deviations in the distributions

of points that satisfy specific constraints.

Examining Fig. 3, we can observe that unitarity and Higgs exclusion limits are the most constraining, while EW precision tests reasonably closely follow the background distribution across all free parameters. We note that unitarity does not exhibit any preference in the trilinear couplings Λ_1, Λ_2 or particle masses, but does show a preference for smaller quartic couplings, particularly for λ_1, λ_2 and λ_7. Higgs exclusion limits on the other hand, exhibit a strong inclination towards negative λ_6 and smaller charged-particle masses m_{C}.

Although no insightful parameter distributions were found for points satisfying STU constraints in Fig. 3, we did observe an interesting pattern when plotting the points' associated free particle masses (m_{N_1}, m_{N_2}, m_{C}) against each other in Fig. 4 (left). The first notable observation is that the regions around the straight line $m_{\mathrm{N}_1} = m_{\mathrm{N}_2}$ have the highest population density of points[7]. Additionally, considering the colour bar, it becomes apparent that points predicting approximately equal masses for all three scalar particles ($m_{\mathrm{N}_1} \approx m_{\mathrm{N}_2} \approx m_{\mathrm{C}}$) are favoured by EW precision tests. A second, more subtle observation is that in the cases where the two neural particle masses are unequal (i.e. not along the diagonal), EW precision tests may still be satisfied if the charged particle mass aligns with the lightest neutral particle mass, i.e., $m_{\mathrm{C}} \approx m_{\mathrm{N}_i}$ where i corresponds to the lightest neutral particle. This alignment can by the vertical and horizontal lines of the same charged particle mass (colour) meeting at the diagonal in Fig. 4 (left). This latter pattern also emerges when considering Higgs exclusion limits in Fig. 4 (right). Once again, vertical and horizonal lines of same colour meet at the diagonal, showing that points producing a charged particle mass that matches the lightest neutral particle mass is preferred when constraining the Higgs sector. However, in this case, one of the neutral particles (and thereby the charged particle) must always remain below approximately 500 GeV.

For the cosmic constraints, we examined roughly 9000 points. Among them, 60 points individually yielding FOPTs, strong FOPTs (S-FOPT) and detectable (as defined by our detectability constraint) FOPTs (D-FOPT) were selected. The PDFs of these points are displayed in Fig. 5. The parameter distributions associated with FOPTs closely follow the background. Any (significant) deviations from the background only become apparent when considering strong and detectable FOPTs, particularly in the λ_1, λ_6 and λ_7 distributions. We observe peaks in the $\lambda_1 \approx -3$ and $\lambda_6 \approx 8$ regions for strong and detectable FOPTs, respectively. Detectable FOPTs, in addition, exhibit a sharp peak in the $\lambda_7 \approx 8$ region. Our plots do not reveal any notable preferences in particle masses when considering the cosmic constraints.

[7]The absence of points satisfying EW-precision tests appearing on the line can be blamed on the parameter space sampling. As mentioned in Sec. 2.6.1, in order for the λ_4 coupling to be real, we require $m^2_{\mathrm{N}_2} > m^2_{\mathrm{C}} > m^2_{\mathrm{N}_1}$ or $m^2_{\mathrm{N}_2} < m^2_{\mathrm{C}} < m^2_{\mathrm{N}_1}$. Hence, for $m_{\mathrm{N}_1} \approx m_{\mathrm{N}_2}$, there exist few m_{C} that will keep λ_4 real. Since all couplings are assumed to be real, a sparse number of points are sampled near the line $m_{\mathrm{N}_1} = m_{\mathrm{N}_2}$ in Fig. 4.

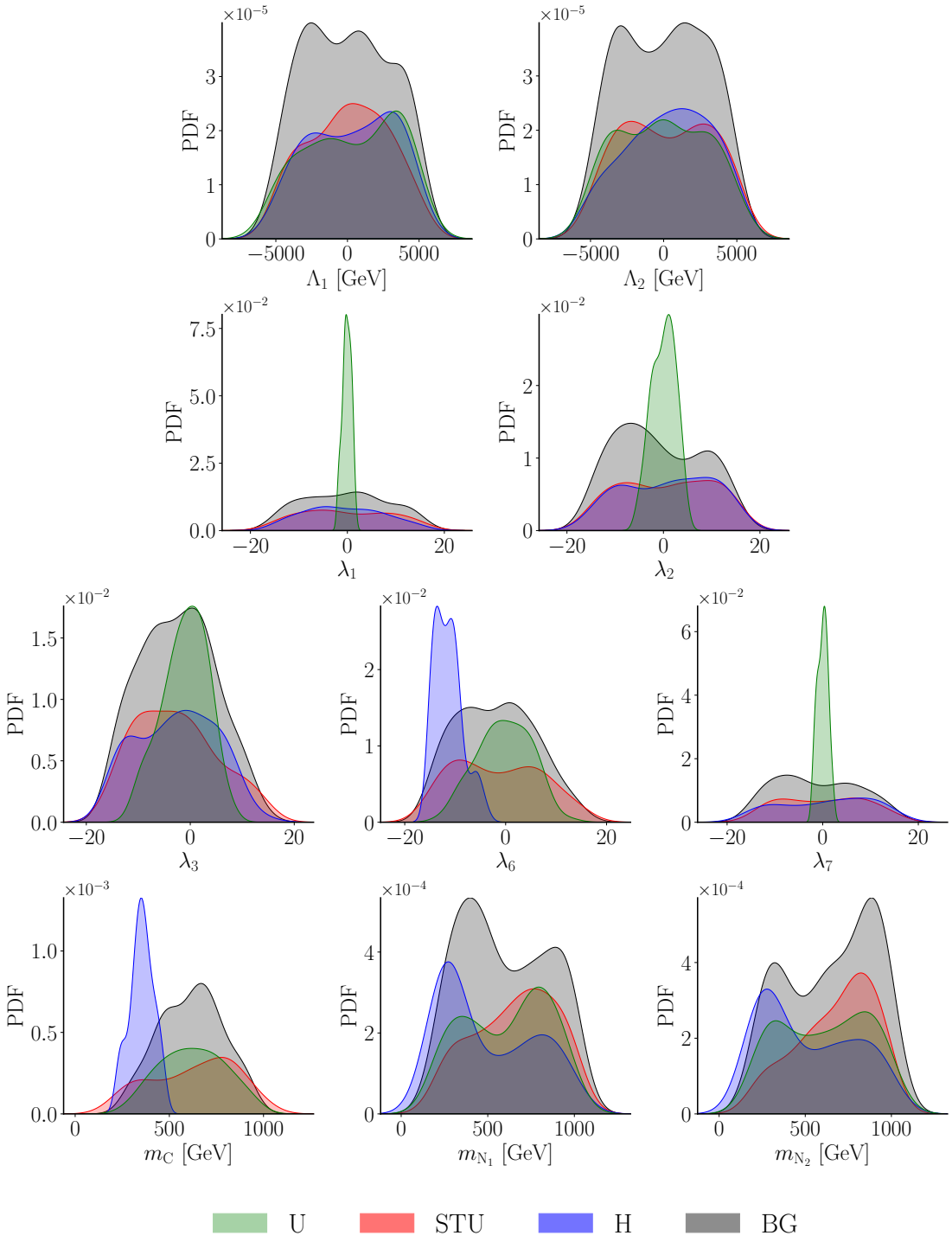

Figure 3: Probability Density Functions (PDFs) of the free parameters Λ_1, Λ_2, λ_1, λ_2, λ_3, λ_6, λ_7, m_{N_1}, m_{N_2} and m_C that satisfy unitarity (U = green), oblique parameter (STU = red) and Higgs exclusion limit (H = blue) constraints, respectively. The distributions should be compared to the sampling distribution (BG = grey). Note that the graphs are not scaled relative to each other.

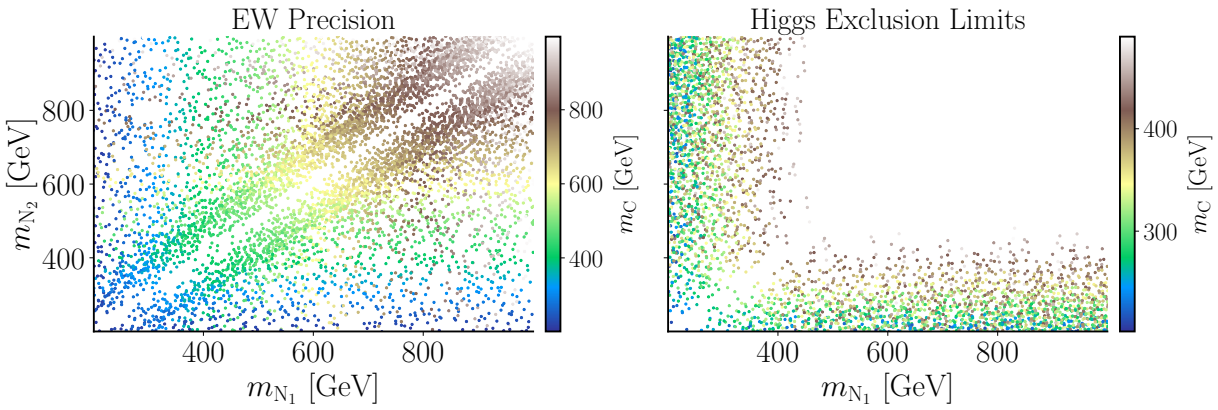

Figure 4: Neutral particle masses m_{N_1} and m_{N_2} plotted against each other with the charged particle mass m_C represented by the colour bar for points satisfying EW precision tests (left) and Higgs exclusion limits (right), respectively.

Fortunately, there are regions for each free parameter where all corresponding distributions overlap. It is important to note that although overlapping distributions is no guarantee that there exist points simultaneously satisfying all constraints, these areas represent potential areas where such points might exist.

6.2 Data collection and ANN training

Comparing the (free) parameter distributions satisfying the different theoretical, collider (Fig. 3) and cosmic (Fig. 5) constraints separately, we take the following parameter space as the region of interest

$$
\begin{aligned}
&-5000\ \text{GeV} < \Lambda_i < 5000\ \text{GeV}, && -3.5 < \lambda_1 < 3.5, && -7.5 < \lambda_2 < 7.5,\\
&-13 < \lambda_3 < 13, && -7.0 < \lambda_6 < -2.5, && -3.5 < \lambda_7 < 3.5\\
&200\ \text{GeV} < m_{N_j} < 1000\ \text{GeV}, && 200\ \text{GeV} < m_c < 550\ \text{GeV}, &&
\end{aligned}
$$

for $i = 1, 2$ and $j = 1, 2$. During data collection, slightly less than 1.5 million points were analyzed. Among the points satisfying unitarity and collider constraints simultaneously, none satisfied our current detectability constraint $h^2\Omega^{\text{peak}} > 10^{-15}$, while only four points had GW peak amplitudes in the region $h^2\Omega^{\text{peak}} \sim 10^{-16}$, far too few for the ANN to train on. Hence, for the sake of training the ANN, the detectability constraint was relaxed by two orders of magnitude, becoming $h^2\Omega^{\text{peak}} > 10^{-17}$, referred to as the "relaxed" constraints [8]. This is done with the intention that by training the ANN on the relaxed constraints, and letting it thereafter produce a large number of such points, we maximize the likelihood to

[8] This is still within the detecting range of DECIGO and BBO (in the appropriate frequency range).

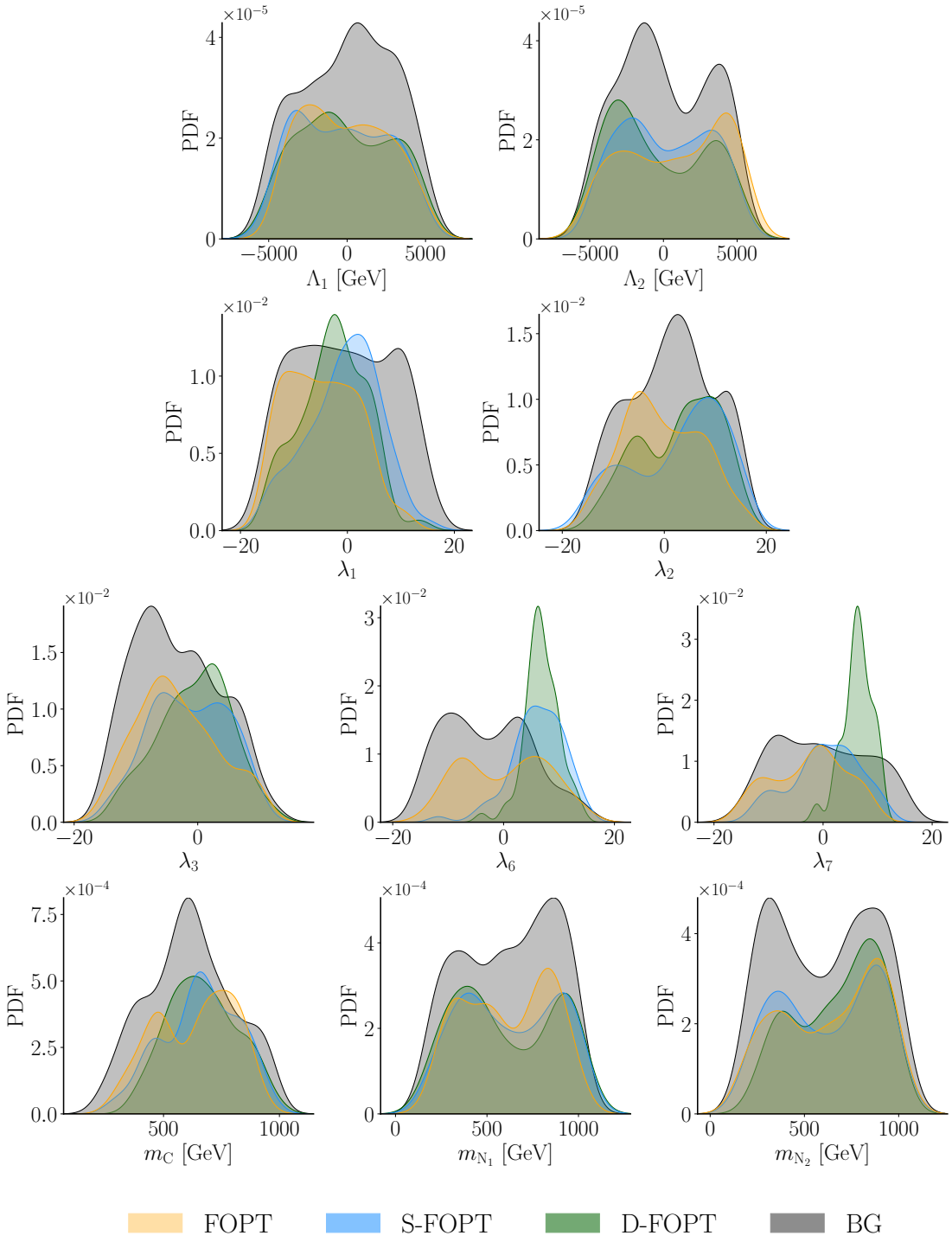

Figure 5: Probability Density Functions (PDFs) of the free parameters Λ_1, Λ_2, λ_1, λ_2, λ_3, λ_6, λ_7, m_{N_1}, m_{N_2} and m_C yielding first-order phase transitions (FOPT = yellow), strong first-order phase transitions (S-FOPT = cyan) and detectable first-order phase transitions (D-FOPT = dark green), respectively The distributions should be compared to the sampling distribution (BG = grey). Note that the graphs are not scaled relative to each other.

Total number of points	1 485 898
Unitarity	152 402
Electroweak precision	186 145
Higgs exclusion limits	111 191
+ Unitarity and collider simultaneously	3 480
+ FOPT	192
+ Strong FOPT	175
+ Detectable FOPT	109

Table 1: A list specifying the number of points satisfying different constraints. Only points satisfying all theoretical and collider constraints simultaneously, specified in the fifth row, are checked for cosmic constraints. The '+' indicates that the points in that particular row have passed all constraints above them. The final row of points are labelled positive for the network training.

finding points that also satisfy our original constraints.

A breakdown of the number of points satisfying each constraint can be found in Tab. 1. Here, we observe that although a reasonably large fraction of points, approximately 10.1% on average, satisfy unitarity, EW precision and Higgs constraints separately, this percentage drops significantly to around 0.23% when requiring that these constraints be satisfied simultaneously. Among these points, only 5.5% yield FOPTs, with majority of them being strong FOPTs however. Applying the relaxed detectability constraint, 109 points are left at the end. Thus, our training data comprises 109 positive points (satisfying theoretical, collider and relaxed cosmic constraints simultaneously) and 1 485 789 negative points. Although the number of positive points may seem small considering the dimensionality of the ANN input space (10) and the complexity of the training data, it still holds potential to enhance our scan.

The first relevant metric for us to measure the performance of the ANN is the accuracy A_{N}. It is the fraction of points that are correctly positively predicted $A_{\mathrm{N}} = \mathrm{TP}/(\mathrm{TP} + \mathrm{FP})$, where "T/F" denotes "True/False" and "P/N" denotes "Positives/Negatives"[9]. Based on Tab. 1, the accuracy of identifying physical points through a random parameter scan is approximately $A_{\mathrm{R}} \approx 7.34 \cdot 10^{-3}$ % [10]. To deem our network successful, we consider A_{R} as the baseline and aim at obtaining a higher accuracy with the ANN. However, we must also ensure that the network does not become overly conservative in its predictions.

[9]E.g., TN is the number of correctly negatively predicted points (i.e., number of points predicted to be negative by the ANN, that in fact are negative), while FP is the number of incorrectly predicted positive points (i.e number of points predicted to be positive by the ANN, which are negative in reality).

[10]Note that it is not completely random in reality. It takes into account our findings from the initial scan, allowing us to probe the parameter space region where we are more likely to find a physical point.

This aspect is measured by the "exhaustiveness" parameter $E = \mathrm{TP}/(\mathrm{TP} + \mathrm{FN})$ (ratio of correctly predicted positive points to the total number of positive points in the system), representing the proportion of positive points the ANN is capable of locating. This allows us to assess if the network is giving its undue attention to certain regions of the parameter space while completely ignoring other parts that also contain positive points. Thus, the objective here is to obtain a network accuracy $A_{\mathrm{N}} > A_{\mathrm{R}}$, while maintaining reasonably high exhaustiveness.

Training the model defined in Sec. 5 provides an ANN accuracy of $A_{\mathrm{N}} \approx 1.74\%$ with exhaustiveness $E \approx 0.84$ [11]. This is an enhancement in accuracy by a factor 237 compared to random search. On top of this, the ANN has a large coverage of the parameter space, indicated by the high E value.

6.3 ANN predictions

We can now utilize the trained ANN to suggest positive points, which we run through the HEP packages. Through this approach, we collected 2537 points satisfying the imposed theoretical, collider and relaxed cosmic constrains, out of which 230 points satisfy our approximate boundedness from below conditions from Sec. 2.6.3. Different intersections of the parameter space containing the collected positive points (excluding the boundedness from below constraint) have been plotted in Fig. 6. In the upper-left graph we observe that the positive points are mainly distributed in the region $\mu_{\mathrm{S}}^2 \lesssim 5 \cdot 10^5$ GeV^2, $\mu_{\mathrm{T}}^2 \lesssim 1.5 \cdot 10^5$ GeV^2 (these mass terms go up to $\mu_{\mathrm{S}}^2 \sim 9 \cdot 10^5$ GeV^2 and $\mu_{\mathrm{T}}^2 \sim 2.5 \cdot 10^5$ GeV^2 in the training data). A dependence between μ_{T}^2 and λ_6 is also seen here, however, this dependence can already be seen in the tadpole Eq. (2.39). The upper-right and bottom-left graphs show clusters of positive points in the λ_1-λ_2 and λ_4-λ_7 planes, respectively, with λ_3 constrained in the range $-5 \lesssim \lambda_3 \lesssim 9$. In the bottom-right graph we observe a similar pattern in the scalar particle masses as in Fig. 4, that is, physical points must always predict one light neutral particle and a light charged particle that approximately align at 200-300 GeV, while the other neutral particle mass is allowed to vary freely in our pre-defined range 200-1000 GeV.

Of the 2537 points above, we identify four points satisfying our original detectability constraint ($h^2\Omega^{\mathrm{peak}} > 10^{-15}$), meeting our initial objective: finding points satisfying unitarity, collider and cosmic constraints that produce GW amplitudes in the sensitivity regions of LISA, DECIGO and BBO. Among the four points, one additionally satisfies the approximate boundedness from below conditions. These points can be seen in Fig. 7, where their GW peak amplitudes $h^2\Omega^{\mathrm{peak}}$ has been plotted against the associated frequencies f^{peak}. Here, we additionally include points with any GW peak amplitude, but that are physical in all other senses (i.e satisfy theoretical, collider constraints and yield strong FOPTs). It

[11] These numbers are found by applying the trained ANN on data which it has not previously seen, known as a validation set.

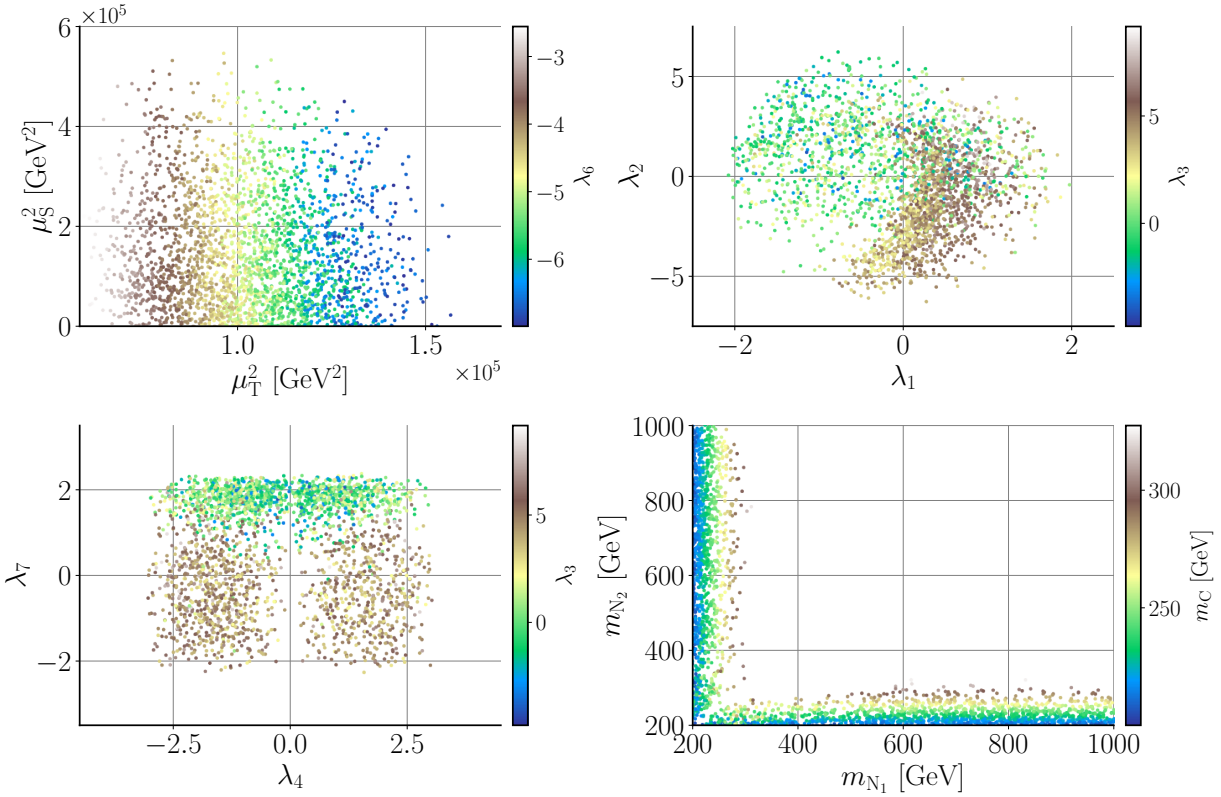

Figure 6: Four intersections of parameter space containing positive points (under relaxed constraints) collected by the trained ANN. These points satisfy unitarity and collider constraints, and produce strong FOPTs with GW peak amplitudes $h^2\Omega^{\text{peak}} > 10^{-17}$.

is important to note that since the ANN is specifically trained to identify physical points with $h^2\Omega^{\text{peak}} > 10^{-17}$, the number of points below the line $h^2\Omega^{\text{peak}} = 10^{-17}$ will be proportionally smaller than the number of points above it when compared to random search. The LISA, DECIGO and BBO sensitivity curves have also been included using the PTPlot code [55, 56].

We observe that the ANN has produced a large number of points that lie above the DECIGO and BBO sensitivity curves. Furthermore, we have even found a point above the LISA sensitivity curve, with a GW peak amplitude $h^2\Omega^{\text{peak}} \sim 10^{-12}$. This value exceeds the largest GW peak amplitude in the training data by four orders of magnitude. We would like to emphasize that while points above the sensitivity curves are promising, the SNR value provides a more accurate measure of detectability, and our detectability results should therefore be interpreted with some caution.

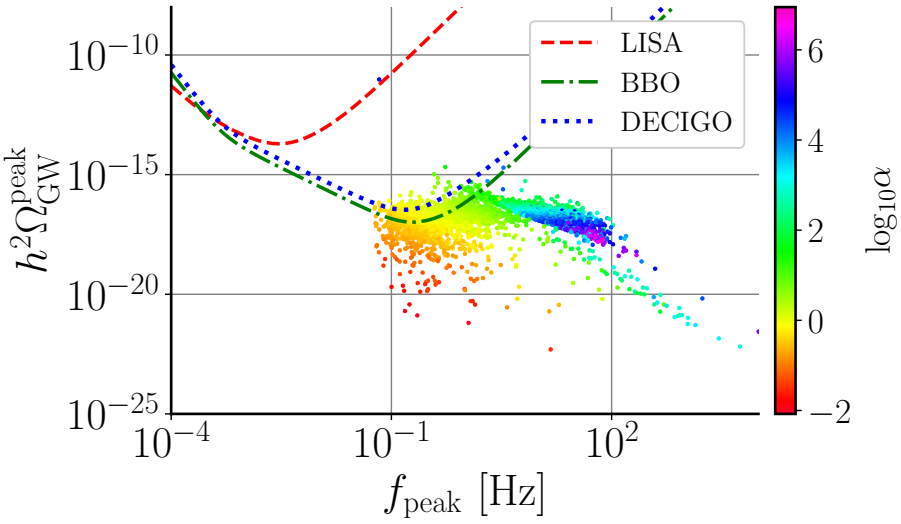

Figure 7: GW peak amplitude $h^2\Omega^{\rm peak}$ plotted against associated peak frequency $f^{\rm peak}$ for physical points (satisfying unitarity and collider constraints, and producing strong FOPTs) with any GW peak amplitude. The Sensitivity curves belonging to LISA, BBO and DECIGO are plotted using the PTPlot tool.

7 Conclusion

This work has served as a trial to investigate the effectiveness of neural networks in probing BSM theory parameter spaces, considering both collider and GW measurement constraints. In order to test the capabilities of the ANN, an EW scale EFT inspired by the QCD-like TC theory was employed as a toy model, taking the form of a $\mathrm{SU}(2)_{\mathrm{W}}$ singlet-triplet extended SM. In addition to the three EW Goldstone bosons and one SM-like Higgs boson, our STESM predicted four additional massive scalar particles, making it a phenomenologically interesting, yet simple, toy model for an investigation of its collider and cosmic impacts. In total, the theory contains ten free parameters: seven Lagrangian couplings, two neutral particle masses and one charged particle mass, which serve as input to the ANN. The space spanned by these parameters is analyzed using the publicly available packages `SPheno`, `HiggsBounds`, `HiggsSignals` and `CosmoTransitions` to apply unitarity, EW precision, Higgs exclusion limit and strong, detectable FOPT constraints. The primary focus of the developed framework is to perform a parameter space scan guided by the suggestions of the neural network, aiming at increasing the accuracy in identifying physical points compared to random search.

Overall, the findings of this thesis have been positive, demonstrating an increased accuracy in locating physical points by a factor larger than 200. This high accuracy was achieved while maintaining a large coverage of parameter space by the network (i.e a high "exhaustiveness" in locating physical points). With random search, we encountered challenges in

identifying points satisfying our original stringent constraints. However, by slightly relaxing these constraints and passing the gathered data to the ANN for training, the neural network successfully isolated points that satisfied our initial requirements. In doing so, we were able to find a large number of physical points potentially detectable by the future planned DECIGO and BBO GW observatories, and even a point potentially detectable by LISA.

While this initial investigation has yielded intriguing results, there is still much development and testing left to be done. Most notably, parts of the script are yet to be generalized to make the framework as model independent as possible. Since the HEP packages which our framework relies on can be applied to a wide range of BSM theories, the framework can in theory be just as model independent. This entails further development efforts. Once the necessary modifications are applied, a proper parameter space investigation of the high-scale QCD-like TC theory, as well as other phenomenologically interesting BSM theories, can be performed using the developed framework. Considering that a large portion of time during this thesis has been dedicated to developing the parameter space scanner using the HEP packages, relatively less time has been allocated for the ANN model selection. Therefore, we believe potential exists for further advancements on the ANN front, particularly in exploring new neural network configurations (e.g. separate neural networks for collider and cosmic constraints) and training techniques. We believe that with further development, the framework can become a useful tool for scanning a wide verity of BSM theory parameter spaces.

8 Acknowledgements

I am incredibly grateful to Roman Pasechnik and António Morais for providing me with such an enjoyable and stimulating project. Their expertise and theoretical input has been invaluable, and I have learnt a lot under their guidance. I am looking forward to continue working with them next term.

Secondly, I would like to express my appreciation to João Gonçalves and Mårten Bertenstam for all of their technical assistance in developing the code in my project. Their dedication in providing suggestions and feedback on the thesis has been immensely valuable and greatly appreciated. They will make fine supervisors in the future.

I would also like to thank Christian Bierlich, for always being available and helping me with the endless amount of technical questions I had this past year.

Finally, I would like to thank my office mates and family. My office mates for creating a fun work environment. Specifically, I would like to thank Erik Rustas for helping me improve my plots. My family for their support and patience during this project. Without their support, this would not be possible.

References

[1] S. F. Novaes. "Standard model: An Introduction". In: *10th Jorge Andre Swieca Summer School: Particle and Fields*. Jan. 1999, pp. 5–102. arXiv: hep-ph/0001283.

[2] José Ignacio Illana and Alejandro Jimenez Cano. "Quantum field theory and the structure of the Standard Model". In: *PoS* CORFU2021 (2022), p. 314. DOI: 10.22323/1.406.0314. arXiv: 2211.14636 [hep-ph].

[3] Eak Paudel. "Problems of Standard Model, Review". In: *BMC Journal of Scientific Research* 4 (Mar. 2022). DOI: 10.3126/bmcjsr.v4i1.42253.

[4] A. D. Sakharov. "Violation of CP Invariance, C asymmetry, and baryon asymmetry of the universe". In: *Pisma Zh. Eksp. Teor. Fiz.* 5 (1967), pp. 32–35. DOI: 10.1070/PU1991v034n05ABEH002497.

[5] José Eliel Camargo-Molina, Rikard Enberg, and Johan Löfgren. "A new perspective on the electroweak phase transition in the Standard Model Effective Field Theory". In: *JHEP* 10 (2021), p. 127. DOI: 10.1007/JHEP10(2021)127. arXiv: 2103.14022 [hep-ph].

[6] R. L. Workman et al. "Review of Particle Physics". In: *PTEP* 2022 (2022), p. 083C01. DOI: 10.1093/ptep/ptac097.

[7] David E. Morrissey and Michael J. Ramsey-Musolf. "Electroweak baryogenesis". In: *New J. Phys.* 14 (2012), p. 125003. DOI: 10.1088/1367-2630/14/12/125003. arXiv: 1206.2942 [hep-ph].

[8] Kenneth D. Lane. "An Introduction to technicolor". In: *Theoretical Advanced Study Institute (TASI 93) in Elementary Particle Physics: The Building Blocks of Creation - From Microfermius to Megaparsecs*. June 1993. DOI: 10.1142/9789814503785_0010. arXiv: hep-ph/9401324.

[9] J. L. Hewett. "The Standard model and why we believe it". In: *Theoretical Advanced Study Institute in Elementary Particle Physics (TASI 97): Supersymmetry, Supergravity and Supercolliders*. June 1997, pp. 3–83. arXiv: hep-ph/9810316.

[10] Tatsu Takeuchi, Will Loinaz, and Aaron K. Grant. "Precision tests of electroweak physics". In: *13th Topical Conference on Hadron Collider Physics*. Apr. 1999, pp. 60–67. arXiv: hep-ph/9904207.

[11] Philip Bechtle et al. "HiggsBounds: Confronting Arbitrary Higgs Sectors with Exclusion Bounds from LEP and the Tevatron". In: *Comput. Phys. Commun.* 181 (2010), pp. 138–167. DOI: 10.1016/j.cpc.2009.09.003. arXiv: 0811.4169 [hep-ph].

[12] Philip Bechtle et al. "*HiggsSignals*: Confronting arbitrary Higgs sectors with measurements at the Tevatron and the LHC". In: *Eur. Phys. J. C* 74.2 (2014), p. 2711. DOI: 10.1140/epjc/s10052-013-2711-4. arXiv: 1305.1933 [hep-ph].

[13] Mark D. Goodsell and Florian Staub. "Unitarity constraints on general scalar couplings with SARAH". In: *Eur. Phys. J. C* 78.8 (2018), p. 649. DOI: 10.1140/epjc/s10052-018-6127-z. arXiv: 1805.07306 [hep-ph].

[14] Florian Staub. "SARAH". June 2008. arXiv: 0806.0538 [hep-ph].

[15] Florian Staub. "Exploring new models in all detail with SARAH". In: *Adv. High Energy Phys.* 2015 (2015), p. 840780. DOI: 10.1155/2015/840780. arXiv: 1503.04200 [hep-ph].

[16] Avelino Vicente. "Computer tools in particle physics". In: (July 2015). arXiv: 1507.06349 [hep-ph].

[17] Philip Bechtle et al. "HiggsBounds – 4: Improved Tests of Extended Higgs Sectors against Exclusion Bounds from LEP, the Tevatron and the LHC". In: *Eur. Phys. J. C* 74.3 (2014), p. 2693. DOI: 10.1140/epjc/s10052-013-2693-2. arXiv: 1311.0055 [hep-ph].

[18] Philip Bechtle et al. "HiggsBounds-5: Testing Higgs Sectors in the LHC 13 TeV Era". In: *Eur. Phys. J. C* 80.12 (2020), p. 1211. DOI: 10.1140/epjc/s10052-020-08557-9. arXiv: 2006.06007 [hep-ph].

[19] Philip Bechtle et al. "HiggsSignals-2: Probing new physics with precision Higgs measurements in the LHC 13 TeV era". In: *Eur. Phys. J. C* 81.2 (2021), p. 145. DOI: 10.1140/epjc/s10052-021-08942-y. arXiv: 2012.09197 [hep-ph].

[20] Werner Porod. "SPheno, a program for calculating supersymmetric spectra, SUSY particle decays and SUSY particle production at e+ e- colliders". In: *Comput. Phys. Commun.* 153 (2003), pp. 275–315. DOI: 10.1016/S0010-4655(03)00222-4. arXiv: hep-ph/0301101.

[21] W. Porod and F. Staub. "SPheno 3.1: Extensions including flavour, CP-phases and models beyond the MSSM". In: *Comput. Phys. Commun.* 183 (2012), pp. 2458–2469. DOI: 10.1016/j.cpc.2012.05.021. arXiv: 1104.1573 [hep-ph].

[22] Carroll L. Wainwright. "CosmoTransitions: Computing Cosmological Phase Transition Temperatures and Bubble Profiles with Multiple Fields". In: *Comput. Phys. Commun.* 183 (2012), pp. 2006–2013. DOI: 10.1016/j.cpc.2012.04.004. arXiv: 1109.4189 [hep-ph].

[23] Andreas Ekstedt, Philipp Schicho, and Tuomas V. I. Tenkanen. "DRalgo: a package for effective field theory approach for thermal phase transitions". In: (May 2022). arXiv: 2205.08815 [hep-ph].

[24] Oliver Witzel. "Review on Composite Higgs Models". In: *PoS* LATTICE2018 (2019), p. 006. DOI: 10.22323/1.334.0006. arXiv: 1901.08216 [hep-lat].

[25] Stefan Scherer and Matthias R. Schindler. "A Chiral perturbation theory primer". In: (May 2005). arXiv: hep-ph/0505265.

[26] H. Sazdjian. "Introduction to chiral symmetry in QCD". In: *EPJ Web Conf.* 137 (2017). Ed. by Y. Foka, N. Brambilla, and V. Kovalenko, p. 02001. DOI: 10.1051/epjconf/201713702001. arXiv: 1612.04078 [hep-ph].

[27] F. Gross. *Relativistic Quantum Mechanics and Field Theory*. 2004.

[28] Roman Pasechnik et al. "Composite scalar Dark Matter from vector-like $SU(2)$ confinement". In: *Int. J. Mod. Phys. A* 31.08 (2016), p. 1650036. DOI: 10.1142/S0217751X16500366. arXiv: 1407.2392 [hep-ph].

[29] Taxén, Jacob. *Chirally Symmetric Technicolor Model: A possible origin of the Higgs Boson*. eng. Student Paper. 2015.

[30] Hristova, Hristina Georgieva. *Cosmological implications of a QCD-like composite Higgs model*. eng. Student Paper. 2021.

[31] Jonathan T. Lenaghan, Dirk H. Rischke, and Jurgen Schaffner-Bielich. "Chiral symmetry restoration at nonzero temperature in the SU(3)(r) x SU(3)(l) linear sigma model". In: *Phys. Rev. D* 62 (2000), p. 085008. DOI: 10.1103/PhysRevD.62.085008. arXiv: nucl-th/0004006.

[32] Nicole F. Bell et al. "A Real Triplet-Singlet Extended Standard Model: Dark Matter and Collider Phenomenology". In: *JHEP* 21 (2020), p. 098. DOI: 10.1007/JHEP04(2021)098. arXiv: 2010.13376 [hep-ph].

[33] Ilya F. Ginzburg and Maria Krawczyk. "Symmetries of two Higgs doublet model and CP violation". In: *Phys. Rev. D* 72 (2005), p. 115013. DOI: 10.1103/PhysRevD.72.115013. arXiv: hep-ph/0408011.

[34] Michael Edward Peskin and Daniel V. Schroeder. *An Introduction to Quantum Field Theory*. Reading, USA: Addison-Wesley (1995) 842 p. Westview Press, 1995.

[35] I. F. Ginzburg and I. P. Ivanov. "Tree-level unitarity constraints in the most general 2HDM". In: *Phys. Rev. D* 72 (2005), p. 115010. DOI: 10.1103/PhysRevD.72.115010. arXiv: hep-ph/0508020.

[36] Philip Bechtle et al. "Probing the Standard Model with Higgs signal rates from the Tevatron, the LHC and a future ILC". In: *JHEP* 11 (2014), p. 039. DOI: 10.1007/JHEP11(2014)039. arXiv: 1403.1582 [hep-ph].

[37] Bertenstam, Mårten. *Searching for signatures of compositeness of the Higgs boson*. eng. Student Paper. 2021.

[38] M. Vojta and T. Dresden. *Thermal and Quantum Phase Transitions*. http://physics.gu.se/~tfkhj/VojtaLesHouches.pdf. [Online; accessed 25-April-2023]. 2015.

[39] Astrid Eichhorn et al. "Universal gravitational-wave signatures from heavy new physics in the electroweak sector". In: *JCAP* 05 (2021), p. 006. DOI: 10.1088/1475-7516/2021/05/006. arXiv: 2010.00017 [hep-ph].

[40] Pau Amaro-Seoane et al. *Laser Interferometer Space Antenna*. 2017. arXiv: 1702.00786 [astro-ph.IM].

[41] Seiji Kawamura et al. "Current status of space gravitational wave antenna DECIGO and B-DECIGO". In: *PTEP* 2021.5 (2021), 05A105. DOI: 10.1093/ptep/ptab019. arXiv: 2006.13545 [gr-qc].

[42] G. M. Harry et al. "Laser interferometry for the big bang observer". In: *Class. Quant. Grav.* 23 (2006). [Erratum: Class.Quant.Grav. 23, 7361 (2006)], pp. 4887–4894. DOI: 10.1088/0264-9381/23/15/008.

[43] K. Kajantie et al. "Generic rules for high temperature dimensional reduction and their application to the standard model". In: *Nucl. Phys. B* 458 (1996), pp. 90–136. DOI: 10.1016/0550-3213(95)00549-8. arXiv: hep-ph/9508379.

[44] João F. Melo. "Introduction to Renormalisation". In: (Sept. 2019). arXiv: 1909.11099 [hep-th].

[45] Djuna Croon et al. "Theoretical uncertainties for cosmological first-order phase transitions". In: *JHEP* 04 (2021), p. 055. DOI: 10.1007/JHEP04(2021)055. arXiv: 2009.10080 [hep-ph].

[46] Valery A. Rubakov and Dmitry S. Gorbunov. *Introduction to the Theory of the Early Universe: Hot big bang theory*. Singapore: World Scientific, 2017. ISBN: 978-981-320-987-9, 978-981-320-988-6, 978-981-322-005-8. DOI: 10.1142/10447.

[47] Lars Husdal. "On Effective Degrees of Freedom in the Early Universe". In: *Galaxies* 4.4 (2016), p. 78. DOI: 10.3390/galaxies4040078. arXiv: 1609.04979 [astro-ph.CO].

[48] Stephan J. Huber and Thomas Konstandin. "Production of gravitational waves in the nMSSM". In: *JCAP* 05 (2008), p. 017. DOI: 10.1088/1475-7516/2008/05/017. arXiv: 0709.2091 [hep-ph].

[49] Chiara Caprini et al. "Science with the space-based interferometer eLISA. II: Gravitational waves from cosmological phase transitions". In: *JCAP* 04 (2016), p. 001. DOI: 10.1088/1475-7516/2016/04/001. arXiv: 1512.06239 [astro-ph.CO].

[50] Mark Hindmarsh et al. "Numerical simulations of acoustically generated gravitational waves at a first order phase transition". In: *Phys. Rev. D* 92 (12 Dec. 2015), p. 123009. DOI: 10.1103/PhysRevD.92.123009. URL: https://link.aps.org/doi/10.1103/PhysRevD.92.123009.

[51] Mårten Bertenstam. *DRalgo to CosmoTransitions*. [Private GitLab repository]. 2023.

[52] TensorFlow Developers. *TensorFlow*. Version v2.12.0. Mar. 2023. DOI: 10.5281/zenodo.7764425. URL: https://doi.org/10.5281/zenodo.7764425.

[53] Bernhard Mehlig. *Machine Learning with Neural Networks*. Cambridge University Press, Oct. 2021. DOI: 10.1017/9781108860604. URL: https://doi.org/10.1017%2F9781108860604.

[54] Michael L. Waskom. "seaborn: statistical data visualization". In: *Journal of Open Source Software* 6.60 (2021), p. 3021. DOI: 10.21105/joss.03021. URL: https://doi.org/10.21105/joss.03021.

[55] Chiara Caprini et al. "Detecting gravitational waves from cosmological phase transitions with LISA: an update". In: *JCAP* 03 (2020), p. 024. DOI: 10.1088/1475-7516/2020/03/024. arXiv: 1910.13125 [astro-ph.CO].

[56] David James Weir. *PTPlot: a tool for exploring the gravitational wave power spectrum from first-order phase transitions*. Version 1.0.2. Aug. 2022. DOI: 10.5281/zenodo.6949107. URL: https://doi.org/10.5281/zenodo.6949107.